

16 Abstract

17 The factors driving variability in rainfall stable water isotopes (the ratios of H_2^{18}O
 18 and ^2HHO to H_2O , expressed as $\delta^{18}\text{O}$, and deuterium excess, d) were studied in a 13-
 19 year dataset of daily rainfall samples from coastal southwestern Western Australia (SWWA).
 20 Backwards dispersion modelling, automatic synoptic type classification, and a statisti-
 21 cal model were used to establish causes of variability on a daily scale; and predictions
 22 from the model were aggregated to longer temporal scales to discover the cause of vari-
 23 ability on multiple timescales. Factors differ between $\delta^{18}\text{O}$ and d and differ according
 24 to temporal scale. Rainfall intensity, both at the observation site and upwind, was most
 25 important for determining $\delta^{18}\text{O}$ and this relationship was robust across all time scales
 26 (daily, seasonal, and interannual) as well as generalizing to a second observation site. The
 27 sensitivity of $\delta^{18}\text{O}$ to rainfall intensity makes annual mean values particularly sensitive
 28 to the year's largest events. Projecting the rainfall intensity relationship back through
 29 ~ 100 years of precipitation observations can explain $\sim 0.2\text{--}0.4\%$ shifts in rainfall $\delta^{18}\text{O}$.
 30 Twentieth century speleothem records from the region exhibit signals of a similar mag-
 31 nitude, indicating that rainfall intensity should be taken into account during the inter-
 32 pretation of regional climate archives. For d , humidity during evaporation from the ocean
 33 was the most important driver of variability at the daily scale, as well as explaining the
 34 seasonal cycle, but source humidity failed to explain the longer-term interannual vari-
 35 ability making d records from this region a poor candidate for reconstructing source hu-
 36 midity.

37 Plain Language Summary

38 In cave deposits, as with several other natural systems, the abundance of heavy iso-
 39 topes of water, oxygen-18 and deuterium, can be used to determine past changes in cli-
 40 mate. This is because the isotopic composition of these systems is linked to that of rain-
 41 fall, while the abundance of heavy isotopes in rainfall is driven by climate parameters
 42 such as temperature and rainfall characteristics. For this to be effective, the factors which
 43 drive rainfall isotopic variability need to be well known. This study uses a 13-year data
 44 set of daily rainfall samples from coastal southwestern Western Australia to better un-
 45 derstand isotopic variability for this region. Oxygen-18 variations here are driven mainly
 46 by rainfall intensity (the amount of rain each day) both according to measurements at
 47 the site and upwind simulations. Deuterium excess, a second order parameter which is
 48 often linked to conditions in the evaporation source region, was well-predicted by source
 49 region humidity at the daily scale but not when aggregated to annual totals. The rela-
 50 tionship between rainfall intensity and oxygen-18 appears to be important over the 20th
 51 century, based on a comparison between observed rainfall and a cave record.

52 1 Introduction

53 In systems where material is sequestered from the environment, for instance speleothem
 54 growth or groundwater infiltration, stable isotope ratios act as one of the markers which
 55 record information about environmental change. Speleothems, that is cave decorations
 56 such as stalagmites and flowstones, record changes in the oxygen isotopic composition
 57 as they grow, and these changes can in turn be linked to changes in rainfall isotopic com-
 58 position (Lachmiet, 2009; Orland et al., 2009; Z. Zhang et al., 2018). Karst regions oc-
 59 cur throughout the mid-latitudes (Chen et al., 2017) meaning that cave records can be
 60 used to infer past changes regional rainfall (Treble, Chappell, et al., 2005; H. Zhang et
 61 al., 2018; Lorrey et al., 2008; Fohlmeister et al., 2012; McCabe-Glynn et al., 2013), in
 62 areas where this is not achievable using materials such as coral and ice. Speleothem use
 63 is widespread, with the SISALv2 database alone containing 691 records of $\delta^{18}\text{O}$ in speleothems
 64 (Comas-Bru et al., 2020). Meanwhile, speleothem fluid inclusions (Vonhof et al., 2006;

65 van Breukelen et al., 2008) and groundwater (Priestley et al., 2020) sample infiltrating
66 rainwater from which hydrogen isotope ratios can be derived.

67 Interpreting these records is not straightforward, even though the link between wa-
68 ter isotope ratios and their drivers is well understood at the laboratory scale. In a closed
69 system, heavier isotopes are concentrated in the more condensed phase according to the
70 temperature-dependent equilibrium fractionation factor (Horita & Wesolowski, 1994; Majoube,
71 1971). When diffusive transport is important, the difference in molecular diffusivity be-
72 tween isotopologues (Merlivat, 1978b) leads to kinetic fractionation. In the climate sys-
73 tem, however, precisely which climatic and atmospheric processes emerge with the strongest
74 link to isotopic variations is less clear.

75 The drivers of isotope variability in the climate system are not even consistent be-
76 tween regions. Towards the poles, oxygen isotopes in ice have been used as an indica-
77 tor of site temperature (Brook & Buizert, 2018); whereas tropical rainfall isotopes have
78 classically been thought of as being controlled by precipitation amount (Dansgaard, 1964).
79 Other important factors include: moisture source (Krklec & Domínguez-Villar, 2014);
80 monsoon activity (Okazaki et al., 2015); the type of precipitation (Aggarwal et al., 2012);
81 the degree of convective organization (Moerman et al., 2013); and trajectories (Deining-
82 er et al., 2016). In the mid-latitudes, where rainfall is driven by synoptic-scale weather sys-
83 tems, water isotopes have also been linked to the type of system. This link is reported
84 both in southern Australia (Barras & Simmonds, 2008, 2009; Treble, Budd, et al., 2005),
85 and elsewhere (Lykoudis et al., 2010; Farlin et al., 2013; Tyler et al., 2016; Wang et al.,
86 2017; Schlosser et al., 2017) and arises because of several factors which systematically
87 differ between systems. These factors include: air mass rainfall history, which drives vari-
88 ability because heavy isotopes are preferentially lost from the atmosphere; and the rel-
89 ative contribution of convective versus stratiform precipitation, which fractionate wa-
90 ter isotopes differently (Aggarwal et al., 2016; Guan et al., 2013; Webster & Heymsfield,
91 2003). The location of a synoptic system, relative to the collection site, can also play a
92 role because of isotopic differences between pre- and post-frontal rain (Aemisegger et al.,
93 2015) and, the sensitivity of isotopes to the time which air parcels spend over land (Good
94 et al., 2014).

95 This study is concerned with southwestern Western Australia (SWWA) in the South-
96 ern Hemisphere midlatitudes, where $\delta^{18}\text{O}$ values in speleothem records (Treble, Chap-
97 pell, et al., 2005) have low frequency variations that are likely to be linked to climate,
98 but a robust understanding of the mechanism is incomplete. Treble, Chappell, et al. (2005)
99 showed that the stable water isotopes measured in SWWA daily rainfall samples, over
100 a one-year study period, are associated with rainfall intensity, but other drivers may also
101 play a role. It is also unclear whether the intensity dependence holds over longer time
102 periods. An understanding of these drivers is particularly important for this region; win-
103 ter rainfall here has dropped significantly since the 1970s (Bates et al., 2008) and plac-
104 ing this in the context of the region’s long-term natural variability is important for fully
105 understanding the change. This is a challenging task because of the region’s strong in-
106 ternal variability, demonstrated in climate models (Cai et al., 2005; England et al., 2006),
107 combined with a short (~ 100 yr) instrumental record (Haylock & Nicholls, 2000).

108 The purpose of this paper, then, is to investigate the factors which influence the
109 abundance of stable water isotopes (^2HHO , H_2^{18}O) in a modern 13 yr record of SWWA
110 rainfall, taking into account day-to-day variations in synoptic types, upstream conditions,
111 and site parameters. In particular, our goal is to identify factors which are important
112 both at the daily, seasonal, and annual scales. This is most relevant to understanding
113 speleothem records from the region, although we expect the measurements to be more
114 widely useful.

115 The remainder of this paper is organized as follows: Sect. 2 describes the charac-
116 teristics of the study region; Sect. 3 introduces the methods used in this study, includ-

ing a Lagrangian trajectory model and statistical methods; Sect. 4 describes the main results and illustrates links between water isotopes and their drivers; and Sect. 5 compares our results with the literature, tests the ability of our interpretation to generalize to another site, as well as summarizing implications for speleothem record interpretation.

2 Regional setting

Southwestern Western Australia (SWWA, Fig. 1), has an average May–October rainfall of up to 850 mm (Bates et al., 2008, Fig. S1), making it a wet and productive region in comparison to the arid inland. Most rain falls during these cooler months, and the total seasonal rainfall is closely related to the number of fronts which cross the coast, which in turn is coupled to the strength and extent of the Hadley-Walker circulation (Rudeva et al., 2019). Along the coastline south of Perth, about 50% of winter rainfall is associated with fronts, which can be accompanied by thunderstorms (Pepler et al., 2020), 20% with cutoff lows (low pressure systems formed at upper tropospheric levels), and the remainder with warm troughs and other synoptic systems (Pook et al., 2012). Further inland, the proportion of frontal rainfall is lower, and the climate is dryer. Other studies, although differing in how synoptic systems are defined (Hope et al., 2014), have generally classified rainfall-bearing systems into similar synoptic types (Raut et al., 2014; Hope et al., 2006) and agree on the importance of frontal rainfall during the rainy winter season. In summer, when the subtropical ridge lies over the region, monthly rainfall of 20 mm or less is typical and frontal rainfall makes up a smaller proportion of the total. Instead, rainfall comes from a mixture of thunderstorms, extratropical cyclones, (Pepler et al., 2020) and warm troughs (Raut et al., 2014). Also more common during summer are the rare, but potentially extreme, events from ex-tropical cyclones (Foley & Hanstrum, 1994).

As well as having a dramatic seasonal cycle, the region’s rainfall has changed on interannual to decadal timescales. Since 1970, the water inflow to Perth’s dams has decreased by half (Power et al., 2005), due to the combined effect of reduced winter rainfall and increased evaporation, and the rainfall intensity distribution has shifted so that light rainfall contributes to a larger fraction of the total (Philip & Yu, 2020). A number of studies, reviewed by Dey et al. (2019), show the rainfall decrease, in winter, is associated with a change in regional circulation including a poleward shift in westerly winds. The resulting decrease in the frequency of strong fronts (Raut et al., 2014) has been related to a significant warming of the Southern Hemisphere troposphere south of 30°S followed by a decrease in the strength of the jetstream, which, in turn, decreases the instability and makes the formation of synoptic disturbances less likely (Frederiksen & Frederiksen, 2007). This is in agreement with a recent study by Lucas et al. (2021), who described a reduction in the intensity of the upward midlatitude circulation branch in the Southern Hemisphere at 30°S. Climate model projections indicate that the drying trend will continue (Bates et al., 2008; Raut et al., 2016).

There are several approaches for determining climate variability before the instrumental record. Changes in rainfall have been inferred from distant measurements of snow accumulation (Zheng et al., 2020), which is possible because of an anticorrelation between SWWA May–October rainfall and snowfall at Law Dome, Antarctica (van Ommen & Morgan, 2010). Speleothem records, an alternative in situ climate proxy, are found in caves which develop in Tamala Limestone (Geoscience Australia & Australian Stratigraphy Commission, 2017), an eolian carbonate deposited in the Middle to Late Pleistocene, ~10–250 ka before present (Smith et al., 2012). Tamala Limestone is extensively distributed along several hundred kilometers of the Western Australian coastline (Fig. 1). Meanwhile, groundwater from the confined aquifers of the Perth Basin (Priestley et al., 2020) has been interpreted as a low-resolution record of infiltration. Both speleothem and ground-

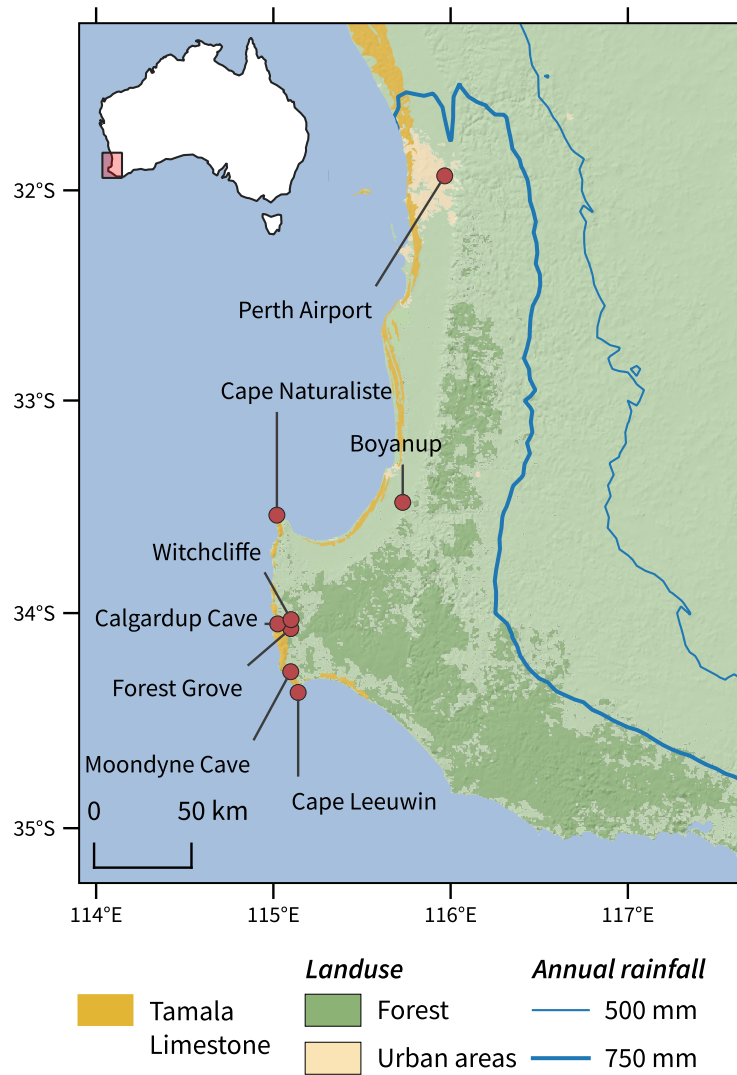


Figure 1. Southwestern Western Australia (SWWA) and locations referenced in the text with: the distribution of Tamala Limestone (a karstic eolianite that occurs along the coast; Geoscience Australia, 2012); land cover (Paget, 2008); and annual mean rainfall (Australian Bureau of Meteorology product IDCJCM004).

168 water records would benefit from a better understanding of the climate drivers of sta-
 169 ble water isotopes.

170 **3 Methods and data**

171 **3.1 Rainfall sampling**

172 Rainfall samples were collected from the Calgardup Cave visitors center within a
 173 forested nature reserve 23 km from the coast (34.0499°S, 115.0246°E, 70 m ASL, Fig. 1).
 174 Samples were collected in a rain gauge consisting of a 203 mm diameter circular funnel
 175 draining into a graduated cylinder. The top of the rain gauge was approximately 0.3 m

176 above the ground and within a small clearing; nearby vegetation was kept clear of the
 177 gauge. The gauge was checked daily at 0900 local time (0100 UTC) and on days with
 178 more than 2 mm of rainfall a sample was collected by filling a 12 ml amber glass bottle
 179 completely to the rim. The sample bottle was sealed using a polypropylene lid with Teflon
 180 tape placed around the thread to improve the seal. Samples were kept refrigerated un-
 181 til analysis. For this study, measurements were included from the years 2006-18 to avoid
 182 including partial years. Occasionally, observers sampled rainfall on days with < 2 mm
 183 of rainfall, and these samples were excluded from analysis. In addition, one outlier was
 184 excluded. This was recorded on 21 April 2010 with an anomalously high $\delta^{18}\text{O}$ of -1.2%
 185 with 52 mm of rainfall, compared to an expected value of about -5% for this amount of
 186 rainfall. Three rain-days later a sample was anomalously low (-5.0% with 4.1 mm of rain-
 187 fall), so it is possible that samples were mislabeled.

188 Isotopes are reported in terms of the isotopologue ratios, R , of oxygen-18 ($\text{H}_2^{18}\text{O}/\text{H}_2\text{O}$)
 189 and deuterium ($^2\text{HHO}/\text{H}_2\text{O}$) relative to Vienna Standard Mean Ocean Water (VSMOW;
 190 IAEA, 2006) in rainwater. We use delta notation where $\delta = R/R_{\text{VSMOW}} - 1$, with $\delta^{18}\text{O}$
 191 and $\delta^2\text{H}$ representing the two isotopologues. Data up to March 2012 were previously pub-
 192 lished (Treble et al., 2013). New data reported here were obtained using a Picarro L2120-
 193 I cavity ring-down spectroscopy analyzer at ANSTO (reported accuracy of $\pm 1.0\%$ for
 194 $\delta^2\text{H}$ and $\pm 0.15\%$ for $\delta^{18}\text{O}$). All data were calibrated against in-house standards calibrated
 195 against VSMOW/VSMOW2 and SLAP/SLAP2.

196 Because $\delta^{18}\text{O}$ and $\delta^2\text{H}$ are strongly correlated, we present $\delta^{18}\text{O}$ results along with
 197 deuterium excess (d), a second-order parameter which characterizes the departure of $\delta^2\text{H}$
 198 from a linear relationship with $\delta^{18}\text{O}$. We follow the most common definition (Dansgaard,
 199 1964) where

$$d = \delta^2\text{H} - 8 \delta^{18}\text{O}. \quad (1)$$

200 Defined this way, d is approximately conserved during Rayleigh distillation, provided that
 201 the ambient temperature is close to 31°C and that Rayleigh distillation does not pro-
 202 ceed too far. Although this is a conventional approach, making our results simple to com-
 203 pare with other studies, it is nevertheless possible for equilibrium processes to change
 204 d and other definitions have been proposed, as discussed by Düttsch et al. (2017). At colder
 205 temperatures, Rayleigh distillation tends to decrease d , as it proceeds because the equi-
 206 librium fraction factors depend on temperature (Horita & Wesolowski, 1994). Since the
 207 heavy isotopes are depleted by Rayleigh distillation, the effect is to produce a positive
 208 correlation between d and $\delta^{18}\text{O}$.

209 Rainfall isotope data are also presented from the Perth Airport Global Network
 210 of Isotopes in Precipitation (GNIP) sampling point, 250 km north of Calgardup Cave,
 211 where rainfall is accumulated monthly for isotopic analysis (Hollins et al., 2018). Ap-
 212 proximately 7 km further inland from Calgardup Cave, there are two automatic weather
 213 stations operated by the Australian Bureau of Meteorology (BoM) at sites 9746 (Witch-
 214 cliffe) and 9547 (Forest Grove). Rainfall measurements are taken from these sites, as well
 215 as the more distant sites: 9503 (Boyanup) and 9519 (Cape Naturaliste).

216 In this paper, the amount of rainfall collected each day is called the ‘rainfall intensi-
 217 ty’, in contrast to ‘rainfall total’ which is the accumulated rainfall over a longer period.
 218 Where averages of $\delta^{18}\text{O}$ and d are computed, these are weighted by rainfall amount un-
 219 less noted otherwise.

220 3.2 Source region diagnostic

221 Several upstream parameters, chosen because of their potential to affect $\delta^{18}\text{O}$ and
 222 d , were diagnosed using two Lagrangian dispersion models. Models were used to com-
 223 pute a backwards plume, or retroplume, from Calgardup Cave on each day with > 2 mm
 224 of rainfall. Backwards plumes are a more realistic generalization of backwards trajec-

225 tories, with advantages discussed by (Stohl et al., 2002). Lagrangian diagnostics have
 226 been widely and successfully used in studies of water isotopes (Pfahl & Wernli, 2008, 2009;
 227 Sodemann et al., 2008, e.g.) including the use of backwards dispersion models (Good et
 228 al., 2014). Quantities related to the evaporation source region were diagnosed from the
 229 source-receptor matrix (Seibert & Frank, 2004) weighted by the instantaneous evapo-
 230 ration rate.

231 In this study, two sets of backwards plumes were generated. The primary set used
 232 FLEXPART version 9.0 (Stohl et al., 2002) with subgrid convective mixing (Forster et
 233 al., 2007) and wind fields from the ERA-Interim reanalysis (Dee et al., 2011). A second
 234 set of backwards plumes was generated using FLEXPART-WRF version 3.1 (Brioude
 235 et al., 2013), forced with a regional atmospheric simulation generated by the Weather
 236 Research and Forecasting model version 3.5.1 (WRF Skamarock & Klemp, 2008). The
 237 WRF model was forced by the CFSR reanalysis (Saha et al., 2010), and configured with
 238 an outer domain which was large enough to contain the backwards plume for approx-
 239 imately 120 h. The second set of plumes was used to verify that the main findings could
 240 be replicated and are not discussed further.

241 Three of the uncertainties in the approach are that: the time of rainfall is only known
 242 to within a 24 h sampling window; the appropriate height for beginning the backwards
 243 plume has to be estimated; and the error in the plume grows as the model is integrated
 244 further back in time. After some experimentation, the beginning time was taken from
 245 the time in the WRF simulation with the largest rain rate, and the starting height was
 246 taken to be the cloud base in WRF, estimated at the height when relative humidity reaches
 247 80%. Then, to verify that the model indeed produces a useful diagnostic, we checked the
 248 correlation between d and humidity relative to saturation at the sea surface tempera-
 249 ture, h_s , as a function of back trajectory length. This is a useful diagnostic because d ,
 250 in vapor, and h_s , at the evaporation site, are strongly correlated (Pfahl & Wernli, 2008)
 251 and we assume that d will be approximately conserved during the conversion of water
 252 vapor into clouds and then rainfall.

253 The correlation between d and h_s grows as the backwards plume increases in du-
 254 ration up to about 48 h, but with no further improvement beyond this point (Fig. S2).
 255 This indicates that both dispersion models have some skill at determining the evapora-
 256 tion conditions at the moisture source, at least up to 48 h before rainfall.

257 3.3 Synoptic classifications

258 On each day, the synoptic type was classified with a Self Organizing Map (SOM),
 259 using SOM-PAK (Kohonen et al., 1996), following the approach described by Hope et
 260 al. (2006). Synoptic types were derived from the 1200 UTC mean sea level pressure (MSLP)
 261 anomaly fields of the ERA-Interim reanalysis on a 0.75° latitude/longitude grid in the
 262 region $90\text{--}130^\circ\text{E}$, $50\text{--}15^\circ\text{S}$. The SOM is an unsupervised classification method, produc-
 263 ing synoptic types that are arranged in a two-dimensional grid. The arrangement of types
 264 into a grid, where similar synoptic types are arranged close to each other, is the main
 265 way in which the SOM differs from other statistical classification techniques (Philipp et
 266 al., 2016). Synoptic classification was only applied to the rainy months (April–October),
 267 due to the presence of seasonally persistent features in the surface pressure field asso-
 268 ciated with the meridional movement of the subtropical high pressure ridge. Training
 269 was performed using data from the years 1979–2018 and grid cells were weighted by area.

270 In addition to the SOM classifications, fronts were detected in the reanalysis fields
 271 and used as an aid to interpret the SOM classifications. The position of fronts was found
 272 using the wind shift method (Simmonds et al., 2011) based on ERA-Interim 3-hourly 10 m
 273 wind fields. This is a straightforward method which is applicable to SWWA (Hope et
 274 al., 2014). It does not produce spurious fronts along the coastline, that are often found
 275 by a more commonly used methods based on the temperature gradients (Pepler et al.,

276 2020). The wind-based method works well to define meridionally elongated fronts, that
 277 are mainly cold fronts, and is particularly well suited for the Southern Hemisphere (Schemm
 278 et al., 2015).

279 3.4 Generalized additive models

280 To combine information from site measurements, backwards plume, and synoptic
 281 type we used Generalized Additive Models (GAMs; Wood, 2017). Separate models were
 282 constructed to predict $\delta^{18}\text{O}$ and d in daily rainfall samples. GAMs, a generalization of
 283 linear regression models, allow the relationships between predictor variables and the re-
 284 sponse variable to be modelled as smooth curves rather than straight lines. In contrast
 285 to many nonlinear machine learning techniques, a benefit of using GAMs is that the re-
 286 lationship between predictor and response variables is simple to visualize, making the
 287 models readily interpretable.

288 The GAM implementation was provided by `mgcv`, a package for R (R Core Team,
 289 2014). Relationships between predictor and response variables are modelled with penal-
 290 ized regression splines in which the smoothness is estimated during the fitting process
 291 using restricted maximum likelihood (REML; Wood, 2011), and models used the iden-
 292 tity link function. In this implementation, predictors which can be modelled with a lin-
 293 ear response are modelled that way, and predictors with insufficient explanatory power
 294 are dropped from the model. The `mgcv` models can also incorporate categorical variables,
 295 allowing the synoptic classification to be included within the same framework.

296 In this study, we also assessed the importance of terms for explaining the obser-
 297 vations on different timescales. As well as allowing the models to drop unimportant terms
 298 (using REML) we followed a procedure where models were constructed term-by-term.
 299 Beginning with an empty model, each candidate term was tested, and the term result-
 300 ing in the best performing model retained. The search for the best term was then repeated
 301 by adding a second term to the model, and so on.

302 The metric for assessing model performance was the 13-fold cross-validated mean-
 303 square error (MSE) applied to daily predictions of $\delta^{18}\text{O}$ or d . To score a model, one year
 304 is held out, and the other years are used to train the model, then the MSE computed
 305 on the held-out year, defined as

$$\text{MSE} = \frac{1}{N} \sum_{i=1}^N (\hat{y}_i - y_i)^2 \quad (2)$$

306 where N is the number of observations, y_i is the i th day's observation and \hat{y}_i is the i th
 307 day's model prediction. This is repeated for all years in the data set, and the MSE is taken
 308 as the average from all the hold-out sets. During model building, terms are added in the
 309 order of the greatest reduction in daily cross-validated MSE.

310 Once the set of models has been obtained, the cross-validated MSE is then recorded
 311 for three groupings: 1. the original, daily, data 2. the mean seasonal cycle during the
 312 rainy months (April–October); and 3. the annual precipitation-weighted means.

313 3.5 Modelled precipitation isotopes

314 In addition to the diagnostic and statistical models described above, we also use
 315 output from a prognostic model: a 40 year simulation of IsoGSM (Yoshimura et al., 2008).
 316 This is one of several atmosphere general circulation models with water isotope tracers
 317 (Risi et al., 2010; Sturm et al., 2005; Schmidt et al., 2007; Lee et al., 2007, e.g.). IsoGSM
 318 is forced with the NCEP/DOE Reanalysis and output from the model is available with
 319 a horizontal resolution of 2.5° .

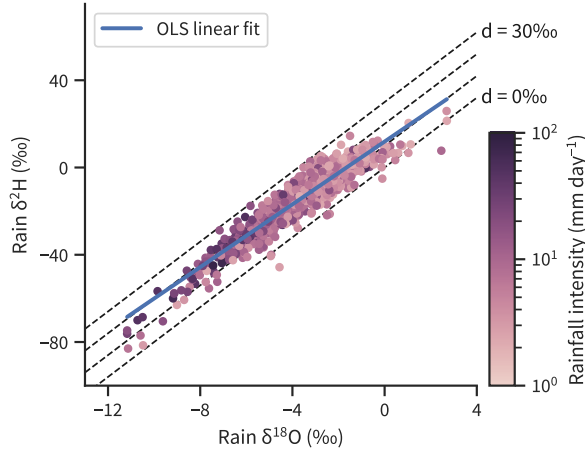


Figure 2. Rainfall $\delta^{18}\text{O}$ and $\delta^2\text{H}$ measured in daily samples from Calgardup Cave visitors centre coloured by the daily rainfall intensity. For comparison, the global average d in precipitation is about 10‰.

320 At other sites, IsoGSM reproduces daily, monthly, and seasonal variability in water
 321 isotope ratios, with more skill at simulating $\delta^{18}\text{O}$ than d (Yoshimura et al., 2008).
 322 At the daily scale, the low accuracy of the model-produced precipitation (that is, the model
 323 may not necessarily produce rain on a rainy day) limits the accuracy of predicted water
 324 isotope ratios.

325 4 Results

326 Our results include a description of the stable water isotopes in Sect. 4.1–4.3 before
 327 moving onto the more interpretive results from statistical and dispersion models in
 328 the later sections.

329 4.1 Daily $\delta^{18}\text{O}$, $\delta^2\text{H}$, and precipitation

330 Over the 13 year monitoring period (2006–18 inclusive, days with $\geq 2 \text{ mm day}^{-1}$ of
 331 rainfall) the precipitation weighted mean $\delta^{18}\text{O}$ was -4.45‰ , d was 15.4‰ , and $\delta^2\text{H}$ was
 332 -20.2‰ . More than 2 mm of rain fell on an average of 90 days each year, and the mean
 333 annual precipitation from these events was 839 mm. The daily isotope samples, when plot-
 334 ted in $\delta^{18}\text{O} \sim \delta^2\text{H}$ space, are strongly correlated and lie about the so-called local me-
 335 teoric water line (LMWL; Fig. 2), with fit parameters given in Tab. S1.

336 There is a tendency for intense rainfall to have lower $\delta^2\text{H}$ and $\delta^{18}\text{O}$ and for low in-
 337 tensity rainfall to both have high $\delta^{18}\text{O}$ and, above -2‰ , depart from the straight line
 338 trend. Deuterium excess for these high $\delta^{18}\text{O}$ samples tends towards the $d = 0\text{‰}$ line,
 339 contrasting to the overall mean d . For comparison, the global meteoric water line (GMWL)
 340 of Craig (1961) lies on the $d = 10\text{‰}$ line.

341 As a result of this tendency for low $\delta^{18}\text{O}$ samples to have lower d , the slope of the
 342 LMWL is lower than the GMWL. The parameters for straight-line fits to the daily rain-
 343 fall samples are shown in Tab. S1, with both ordinary least-squares (OLS) and precipi-
 344 tation weighted least squares (WLS, Hughes & Crawford, 2012). Taking uncertainty into
 345 account, the slope of the LMWL at Calgardup Cave is indistinguishable from the Perth

346 Airport LMWL, but there is an offset between the two sites since the intercept dif-
 347 fers by about two standard deviations.

348 As noted in Sect. 3.1, the temperature-dependence of equilibrium fractionation would
 349 lead to an increase in d with $\delta^{18}\text{O}$. Here we see the opposite trend, which is indicative
 350 of non-equilibrium processes becoming relatively more important during light rainfall.

351 4.2 Seasonal cycle

352 The composite seasonal cycle of $\delta^{18}\text{O}$, d , and P has been published previously for
 353 Perth (Hollins et al., 2018; Liu et al., 2010) and the seasonal cycle at Calgardup is broadly
 354 similar (shown later in Fig. 8, but also Fig. S1). The similarity is consistent with iso-
 355 topes at the two sites being driven by similar factors.

356 The $\delta^{18}\text{O}$ minimum occurs in May or June, earlier than the July peak in rainfall.
 357 January stands out as an exception with anomalously low—and variable—rainfall $\delta^{18}\text{O}$ when
 358 compared with the surrounding months, likely because of the occurrence of rare, but in-
 359 tense, rainfall events. Deuterium excess, d , also has a strong seasonal cycle which mir-
 360 rors $\delta^{18}\text{O}$, peaking in the rainy months. Unlike $\delta^{18}\text{O}$, summer variability is not especially
 361 pronounced.

362 4.3 Annual mean time series

363 Rainfall $\delta^{18}\text{O}$, aggregated to annual precipitation-weighted averages, follows an over-
 364 all decreasing trend, which is present at both Calgardup Cave and Perth as well as in
 365 IsoGSM model output (Fig. 3). From 2009 onwards, however, there is no statistically
 366 significant trend. Comparison with longer term model output, and earlier data from Perth,
 367 (Hollins et al., 2018) indicates that 2006–08 were anomalously high, compared to the long-
 368 term average. The annual-mean d (Fig. 3b) shows similar trends at Perth and Calgardup
 369 Cave, but the IsoGSM simulations are unable to reproduce the observed trends. There
 370 is no consistent trend in d if the first three years are excluded.

371 On average, annual $\delta^{18}\text{O}$ values are 0.61‰ higher at Perth implying a meridional
 372 gradient in $\delta^{18}\text{O}$ of 0.29‰ per degree of latitude. This agrees with a persistent feature
 373 of isotope enabled GCMs which simulate a $\delta^{18}\text{O}$ maximum over the Indian Ocean north
 374 of Perth, near 30°S and under the descending branch of the Hadley Cell, with decreas-
 375 ing values towards the pole (Werner et al., 2011; Lee et al., 2007; Noone & Simmonds,
 376 2002; Risi et al., 2012). The offset between mean values for Perth and Calgardup Cave
 377 shows no trend through time, implying that the meridional gradient has remained con-
 378 sistent over the monitoring period.

379 Annual mean departures from the trend are not consistent between sites (Fig. 3a),
 380 suggesting that $\delta^{18}\text{O}$ anomalies are related to local processes. At least in part, the low
 381 correlation between sites is because annual mean $\delta^{18}\text{O}$ is particularly sensitive to the heav-
 382 iest events of the year, shown by plotting four similar time series in which the heaviest
 383 1–4 rainfall events from each year are excluded. Excluding the heavy events shifts the
 384 mean $\delta^{18}\text{O}$ higher and, in years like 2015 and 2018, can change annual means from anoma-
 385 lously low to high. As with any rainfall event, these events will be sampled differently
 386 by the two monitoring sites (Good et al., 2014), so stochastic variability is a major con-
 387 tributor to the annual precipitation-weighted mean $\delta^{18}\text{O}$. In contrast to $\delta^{18}\text{O}$, the in-
 388 terannual variability in d is not as strongly affected by these intense rainfall events (Fig. 3b),
 389 so the annual-mean difference between Perth and Calgardup Cave time-series are not
 390 as sensitive to stochastic variability.

391 To examine the factors which drive these long-term changes, and the seasonal cy-
 392 cle, we analyze the conditions on each rainy day in the following sections.

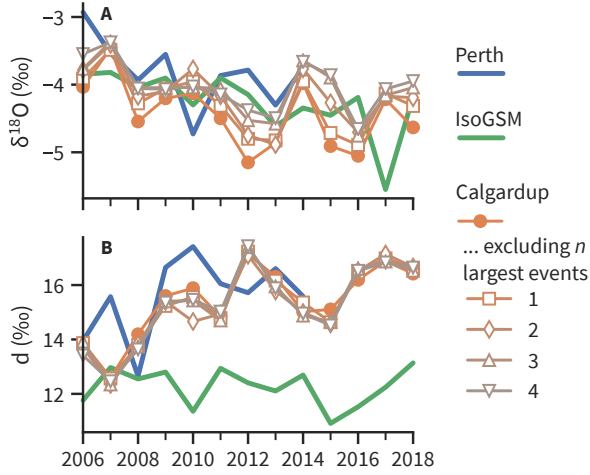


Figure 3. Annual precipitation-weighted mean $\delta^{18}\text{O}$ and d from Calgardup Cave and Perth. As well as showing the entire dataset, the annual mean values for Calgardup are also computed after incrementally leaving out the four largest daily rainfall accumulations, illustrating the sensitivity of interannual $\delta^{18}\text{O}$ variations to a few events. Results from the IsoGSM isotope-enabled general circulation model are also shown.

393

4.4 Synoptic systems

394

Self organizing maps (SOMs) were used to classify synoptic regimes. We identified 35 synoptic types using MSLP fields from ERA-Interim, and each day was associated with one of types shown in Fig. 4. Supplementary interpretation is provided by the frontal density and 500 hPa height fields in Fig. S3, and Fig 5 summarizes several observations according to synoptic type.

396

397

398

Although the SOM is not derived directly from frontal information, the location of fronts is related to the surface pressure field and the synoptic types are therefore associated with front positions. The top two rows in the SOM are most strongly associated with the presence of rain-bearing cold fronts directly over SWWA, while the sequence around the outside edge of the SOM, A4 ··· A1 ··· E1, tracks the progress of cold fronts beginning offshore to the west and moving east across the region. This is a common occurrence, and appears as a path with high transition probabilities in Fig. 5A. Types in the top left are more pre-frontal rainfall, while types in the top right are post-frontal.

399

400

401

402

403

404

405

406

Synoptic types away from the top rows are not as strongly associated with frontal rainfall (Fig. S3); although fronts are detected they are generally away from SWWA. Notably, the pressure pattern for classes A5, A6 resembles a trough, associated with moisture transport from the northwest, and A7 is a blend between a trough and cutoff low. These three classes, in general, are related to upper-tropospheric processes with fronts being detected too far to the west to be responsible for rainfall.

407

408

409

410

411

412

As shown in Fig. 5 synoptic types are a reasonable predictor of rainfall properties, several of which show a strong dependence on SOM classification. In particular, the wettest class (A1) has a rainfall probability of 66%, much higher than the driest class with 5% probability of rain (Fig. 5d). Rainfall intensity (Fig. 5c) is also sensitive to synoptic type, with column A showing the most intense rainfall, especially for classes A5 and A6. Although these non-frontal classes are associated with heavy rain, and A6 accounts for the highest total precipitation, frontal events are responsible for more rainfall overall as they

413

414

415

416

417

418

419

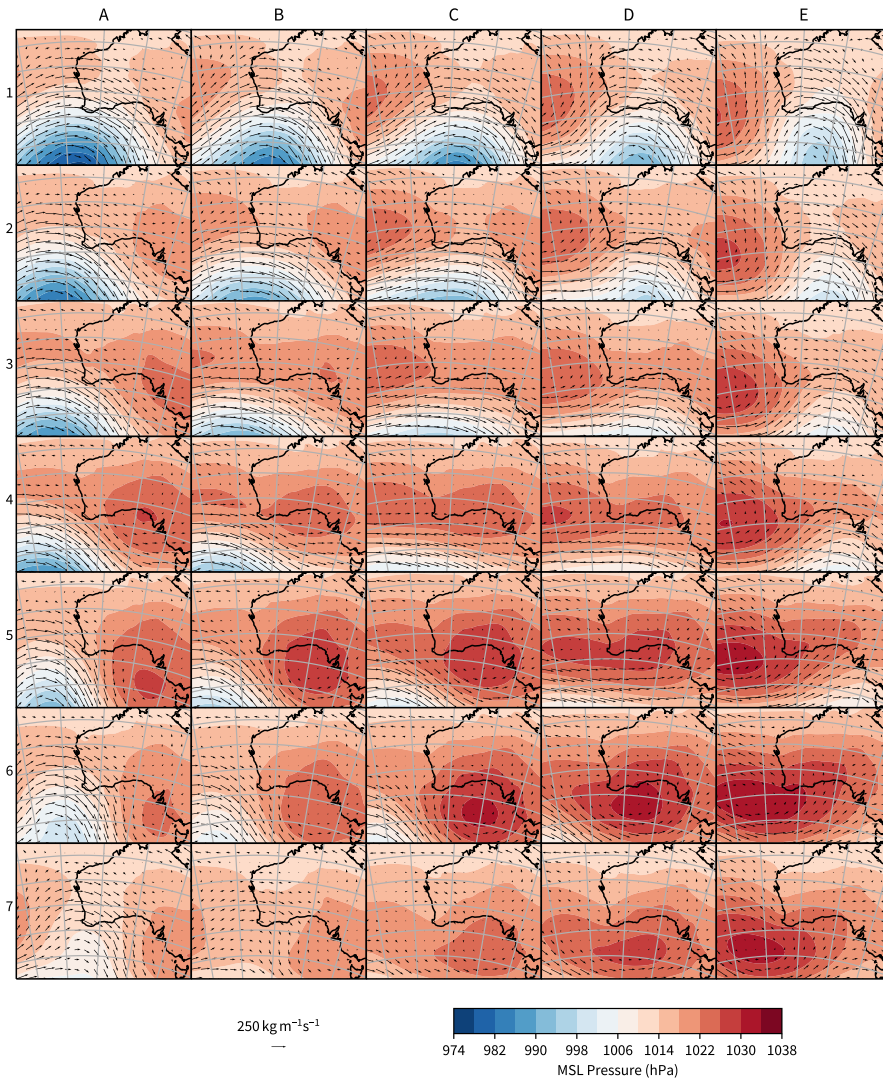


Figure 4. SOM-derived synoptic types, with mean-sea-level pressure and vertically-integrated water vapor transport.

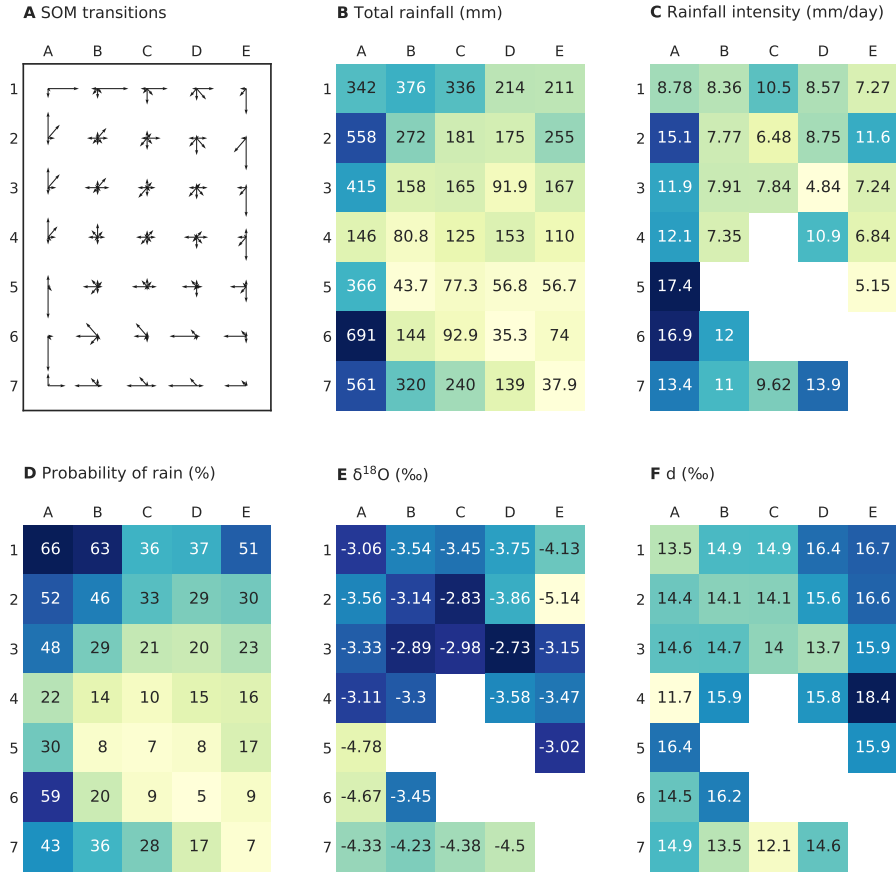


Figure 5. Rainfall, isotope, and SOM properties, 2006-18, by synoptic type. Panels show: **A** relative transition probability (longer arrows show more likely transitions); **B** accumulated precipitation; **C** rainfall intensity (mean rainfall per day); **D** probability of rainfall; **E** arithmetic mean $\delta^{18}\text{O}$; **F** arithmetic mean deuterium excess, d . Colors are used to highlight patterns in the data, the number of days in each class ranges from 51 to 101, and cells with less than 10 observations are left blank in panels C, G, and H.

420 occupy a larger number of classes. Based on manual classifications, Pook et al. (2012)
 421 also found that fronts were responsible for most winter rainfall.

422 Water isotopes show a weaker dependence on synoptic type than precipitation it-
 423 self, but a relationship nevertheless exists (Fig. 5e and 5f). For $\delta^{18}\text{O}$, frontal rainfall shows
 424 a trend towards lower $\delta^{18}\text{O}$ and higher d after the passage of the front, seen in the top
 425 row of these figures. Another pattern revealed by the SOM is that non-frontal rainfall
 426 is lower in $\delta^{18}\text{O}$. Trends in d (Fig. 5f) are in the opposite direction, with the non-frontal
 427 class A5 having higher d than the frontal rainfall classes A1-A3.

428 These observations are consistent with other studies (Treble, Budd, et al., 2005;
 429 Barras & Simmonds, 2008) which have demonstrated, in the Australian region, that dif-
 430 ferent types of synoptic systems can have distinct isotopic signatures, an effect which is
 431 replicated at sites elsewhere in the world (Baldini et al., 2010; Scholl et al., 2009). In par-
 432 ticular, the anomalously low rainfall $\delta^{18}\text{O}$ observed from intense low pressure systems
 433 lying off the eastern coast of Australia (Crawford et al., 2017) is a similar finding to the
 434 low $\delta^{18}\text{O}$ and intense rainfall seen in classes A6 and A7.

435 The SOM analysis, while showing an association between synoptic types and iso-
 436 topes, does not by itself identify the reasons behind the association. Furthermore, although
 437 there is a relatively large difference between frontal and non-frontal rainfall, $\delta^{18}\text{O}$ dif-
 438 fering by 1–1.7‰, this difference is not large enough to explain the year-by-year variabil-
 439 ity (Fig. 3). Year-by-year changes can reach 1‰, meaning that rainfall would need to
 440 switch from almost exclusively frontal rainfall to non-frontal to explain the changes in
 441 annual mean $\delta^{18}\text{O}$, and this is not something which is observed. In the next section, up-
 442 stream conditions, diagnosed from dispersion modelling, are combined with site-based
 443 observations and synoptic types to gain more insight into the underlying processes.

444 4.5 Generalized additive model for $\delta^{18}\text{O}$

445 Generalized additive models (GAMs) trained to predict daily rainfall $\delta^{18}\text{O}$ are shown
 446 in Fig. 6. These curves are the model’s ‘smooth terms’, that is the smooth functions ex-
 447 pressing the relationship between predictor variables and the response variable. Two mod-
 448 els are shown, one with synoptic types (trained on data from the wet months, Apr–Oct)
 449 and another without synoptic types (trained on data from the entire year). In this fig-
 450 ure, smooth terms are ordered by their explained deviance (Wood, 2006); a measure of
 451 importance for predicting daily $\delta^{18}\text{O}$. Metrics for judging the importance of terms are
 452 shown in Fig. 7.

453 For predictions of daily $\delta^{18}\text{O}$, the most important smooth terms in this model are:
 454 the locally-recorded rainfall intensity, P ; the mean rainfall intensity along the retroplume,
 455 \bar{P} ; and then source humidity, h_s relative to the sea surface temperature. Local rainfall
 456 intensity is the best predictor of daily $\delta^{18}\text{O}$, the seasonal cycle, and year-to-year vari-
 457 ability (Fig. 7), it follows a relationship which is close to $\delta^{18}\text{O} \propto \log(P)$. Adding the
 458 retroplume rainfall intensity improves the model’s fit to interannual variability, by al-
 459 most as much as P , but does not affect its fit to the seasonal cycle. The third term, h_s
 460 is defined as the humidity in the evaporation region, within the lowest model level, re-
 461 lative to the sea surface temperature, and weighted by evaporation rate. Source humid-
 462 ity is important for the $\delta^{18}\text{O}$ seasonal cycle, but not interannual variability. Indeed, the
 463 inclusion of h_s increases the model error for the prediction of interannual variability.

464 Remaining terms do not make a major difference to the model’s predictive abil-
 465 ity at interannual scales (Fig. 7). Nevertheless, the starting latitude and longitude of the
 466 plume, along with the source temperature and retroplume overland fraction, are detected
 467 in the model as having an influence on $\delta^{18}\text{O}$, and are discussed further in Sect. 5.

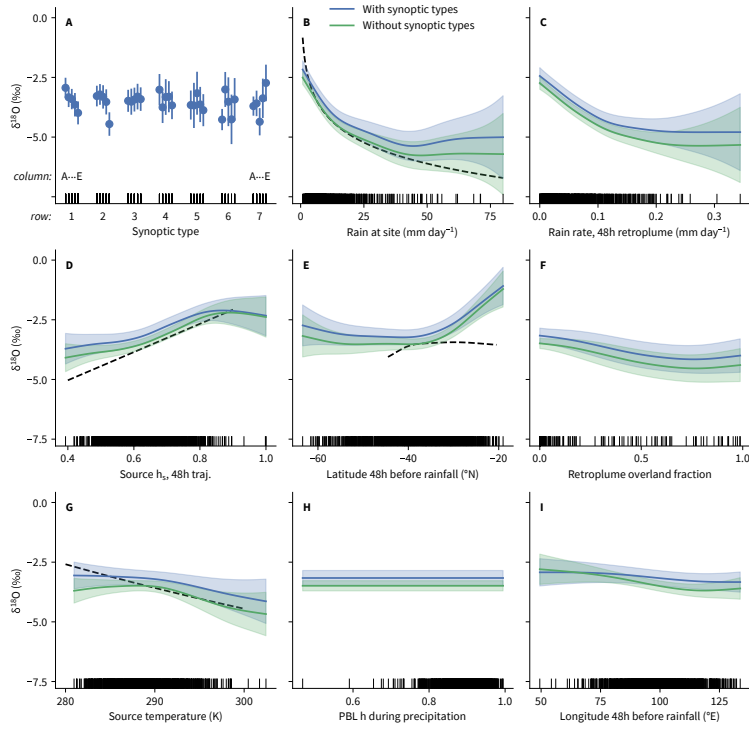


Figure 6. Categorical and smooth terms for a GAM predicting daily $\delta^{18}\text{O}$. The categorical term is shown first, then smooth terms are ordered from the highest to lowest explained deviance. Error bars or shading indicates the 95% confidence interval. Upward ticks on the x -axis of each plot indicate measurements and black dashed lines show other relationships: **B** $\log P$; **D** kinetic fractionation (Merlivat & Jouzel, 1979; Benetti et al., 2014); **E** $\delta^{18}\text{O}$ latitudinal variation in Indian Ocean surface waters (LeGrande & Schmidt, 2006); **G** equilibrium fractionation factor dependence on temperature (Horita & Wesolowski, 1994).

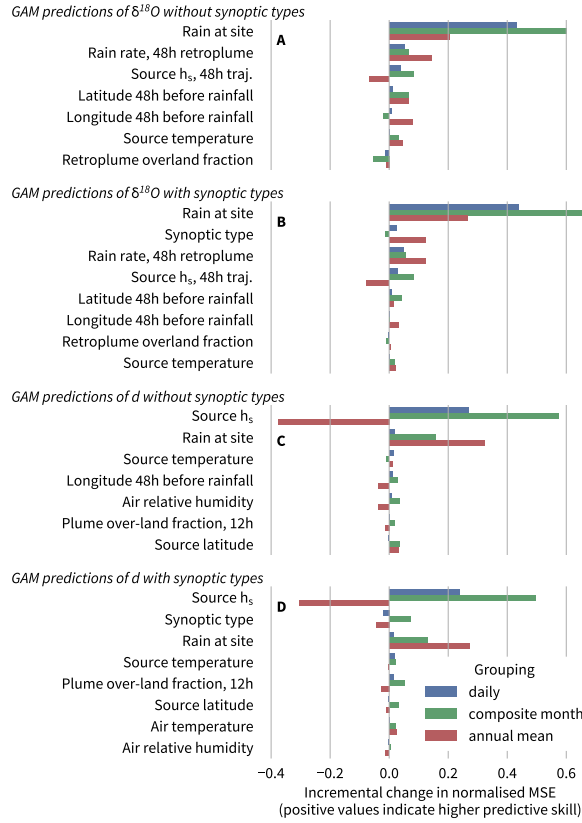


Figure 7. Prediction accuracy of GAM: **A** $\delta^{18}\text{O}$ predictions; **B** like A, but the additional ‘synoptic type’ predictor; **C** d predictions; **D** like C, but with synoptic types. Plots show the improvement in the cross-validated mean squared error (MSE) compared with a simpler model without that term, starting from a model which predicts the mean. MSE is normalized the by MSE of the ‘constant value’ model. In each category, three precipitation-weighted groupings are considered: 1. the ungrouped daily data; 2. monthly groups for a composite year; and 3. annual totals.

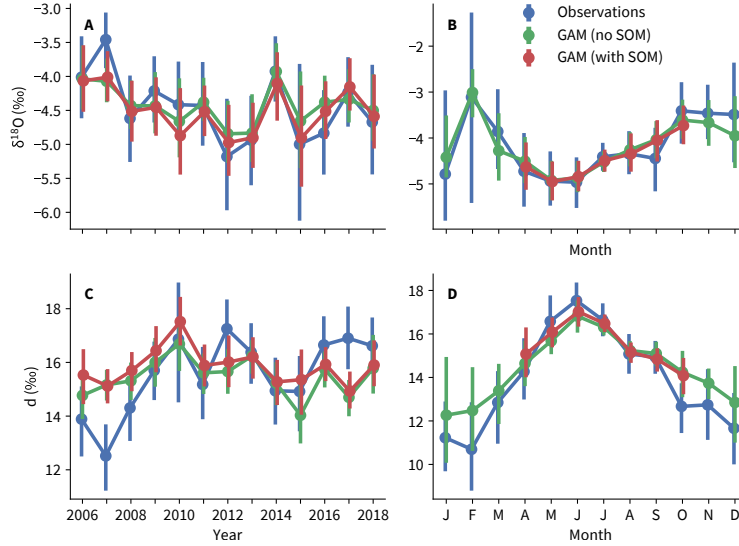


Figure 8. Precipitation-weighted GAM predictions versus observations: **A** annual $\delta^{18}\text{O}$; **B** seasonal $\delta^{18}\text{O}$; **C** annual d ; and **D** seasonal d . Error bars show the 95% confidence interval from bootstrapping daily values.

468 Despite being statistically-significant, including synoptic types as a predictor vari-
 469 able does not appreciably improve the overall model performance (Fig. 7), suggesting
 470 that synoptic types contain redundant information already contained in the smooth terms.
 471 The shape of the smooth terms is also insensitive to the presence of synoptic types, as
 472 seen in Fig. 6 where the GAM with synoptic types has similar smooth terms to the GAM
 473 without. There are also similarities in the patterns of Fig. 6a, which show the effect of
 474 synoptic type marginalized for the effect of other variables, to the patterns in Fig. 5e which
 475 showed the mean $\delta^{18}\text{O}$ in each synoptic type.

476 A comparison of GAM predicted oxygen isotopes with observed timeseries is shown
 477 in Fig. 8a and 8b showing that the GAM successfully tracks $\delta^{18}\text{O}$ interannual variabil-
 478 ity and the seasonal cycle.

479 In summary, the combination of the GAM analysis with synoptic types supports
 480 the conclusions of earlier studies which have found that isotopic composition is related
 481 to synoptic types, but it also shows that there are underlying continuous variables which
 482 explain the isotopic composition, for this region, without needing to incorporate synop-
 483 tic types. The continuous predictor variables have the advantages that they can be used
 484 in all months of the year and are less likely to cause over-fitting.

485 4.6 Generalized additive model for deuterium excess

486 Deuterium excess, d , differs from $\delta^{18}\text{O}$ both in terms of which predictors are im-
 487 portant, and how well a GAM trained on daily data is able to predict interannual vari-
 488 ability. As with $\delta^{18}\text{O}$, our approach was to train a GAM using daily data and then use
 489 this model to make predictions aggregated over longer periods. Next, another GAM was
 490 trained with the additional predictor of synoptic types.

491 The leading predictor of daily d is source humidity, h_s relative to saturation at the
 492 sea surface. It is followed by rainfall intensity, P . Compared with h_s , P only weakly im-
 493 proves the MSE at the daily scale (Fig. 7c) but it is the term which improves the annual-

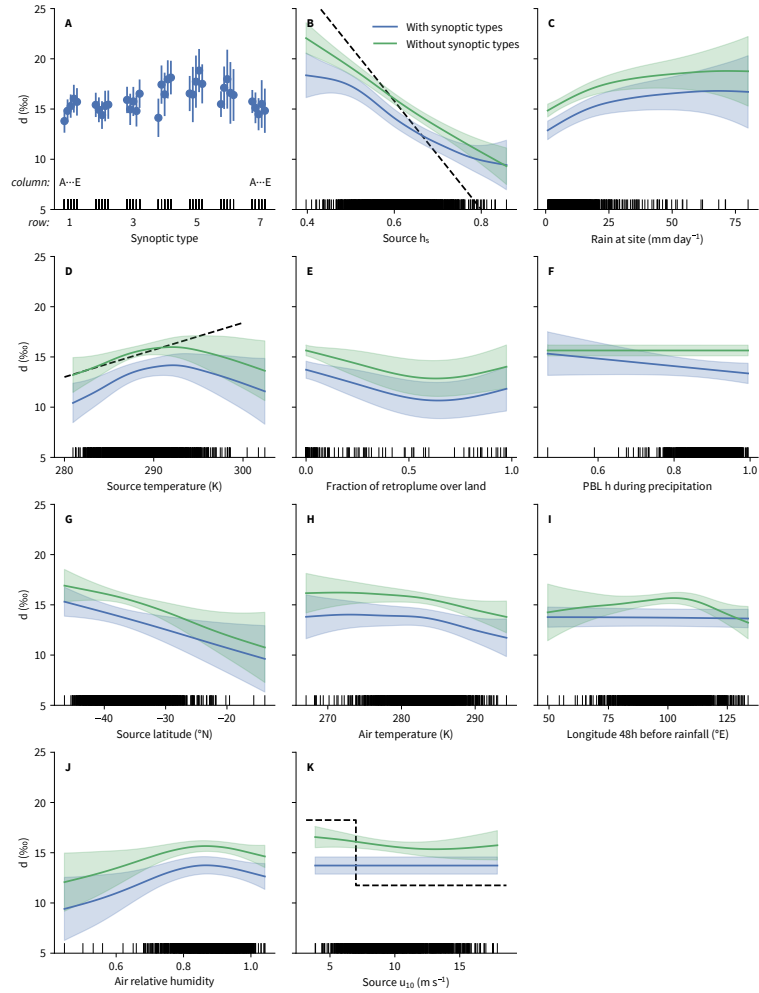


Figure 9. Smooth terms for GAM predicting daily d . Other relationships shown are: **B** empirical relationship from Pfahl and Sodemann (2014); **D** empirical relationships from Bonne et al. (2019); **K** parameterisation from Merlivat and Jouzel (1979) at $h_s = 0.6$ (Benetti et al., 2014).

494 mean predictions the most as well as contributing to a better prediction of the seasonal
495 cycle.

496 The effect of adding synoptic types to the d model, which also means restricting
497 the model to rainy months, is shown in Fig. 7d. Synoptic type, although statistically im-
498 portant according to the REML test, fails to improve the cross-validated MSE at the daily
499 or interannual time scales. As with $\delta^{18}\text{O}$, the information introduced to the model by
500 the synoptic types is redundant, and harms the cross-validated performance of the model,
501 possibly because the large number of categories promotes over-fitting.

502 Of all the factors in this analysis, however, it is the source humidity which stands
503 out. It is strongly linked to d at the daily scale, it is apparently the main driver of the
504 observed seasonal cycle, but it produces a very poor model of interannual variability—
505 one which has a larger error than a model without h_s . When plotted alongside obser-
506 vations, the annual mean predictions of d (Fig. 8c) show that, in contrast to the case of
507 $\delta^{18}\text{O}$, the GAM is unable to follow the overall increasing trend in observed rainfall d , even
508 though it is largely successful at reproducing the seasonal cycle. The GAM predictions
509 start above the observations and then are biased low by the end of the observation pe-
510 riod (model residuals are shown more clearly in Fig. S4). An explanation for this appar-
511 ent contradiction is that there is a missing term which is correlated with both h_s and
512 $\delta^{18}\text{O}$ at the annual-mean timescale.

513 5 Discussion

514 5.1 Physical processes driving $\delta^{18}\text{O}$

515 The process with the strongest link to rainfall $\delta^{18}\text{O}$ was the rainfall intensity, both
516 that measured at the site (P) and along the retroplume (\bar{P}). Although P and \bar{P} are closely
517 related conceptually, they are only moderately correlated ($R = 0.33$) and it is possi-
518 ble that both are imperfect proxies of the same underlying factor driving isotopic frac-
519 tionation, such as the proportion of water remaining in the system (Lee & Fung, 2008)
520 in analogy with Rayleigh distillation, or the relative importance of moisture convergence
521 versus local evaporation, which has been described in steady-state over an idealized trop-
522 ical ocean (Moore et al., 2014).

523 Rainfall intensity, that is rainfall measured each day, has a stronger association with
524 $\delta^{18}\text{O}$ than does total monthly precipitation, in agreement with Fischer and Treble (2008)
525 who studied monthly $\delta^{18}\text{O}$ data from Perth and a short record of daily measurements
526 from Cape Leeuwin. Also similar is that Fischer and Treble (2008) found a nonlinear re-
527 lationship between precipitation and $\delta^{18}\text{O}$, using $\delta^{18}\text{O} \propto P^{\frac{1}{2}}$. In our data set, due to
528 scatter, $\delta^{18}\text{O} \propto P^{\frac{1}{2}}$ fits the data almost as well as $\delta^{18}\text{O} \propto \log(P)$, and we plot the log
529 form mainly out of preference because of its appearance in Rayleigh distillation (Eriksson,
530 1965) and also the use of a log transformation when $\delta^{18}\text{O}$ is regressed against moisture
531 residence time, τ . Aggarwal et al. (2012) found that $\delta^{18}\text{O} \propto \tau = \log(Q/P)$ where Q
532 is the total column water vapor and P is the long-term mean precipitation rate. In our
533 data, variability in Q is small enough that $\log(P/P_0)$ is strongly correlated with τ ($R =$
534 -0.94 , Q from ERA-Interim) and there is no advantage in using τ .

535 Source humidity, h_s affects $\delta^{18}\text{O}$ through kinetic fractionation. The relationship
536 determined by the GAM is similar to the expression for kinetic fraction used by Benetti
537 et al. (2014), as shown by the dashed line in Fig. 6d. In contrast, the relationship be-
538 tween latitude and $\delta^{18}\text{O}$ (Fig. 6e) does not follow the meridional variation in Indian Ocean
539 surface water $\delta^{18}\text{O}$ (LeGrande & Schmidt, 2006). Fischer and Treble (2008) also reported
540 a difference in $\delta^{18}\text{O}$ between airmasses travelling equatorward or poleward, but our re-
541 sults suggest that isotopic differences in the source waters are not responsible. Instead,
542 there are multiple co-varying parameters which may obfuscate the direct effect of source
543 water $\delta^{18}\text{O}$; latitude is strongly correlated with the oceanic source temperature ($R =$

0.91), wind speed ($R = -0.61$), and humidity ($R = 0.48$). In addition, there is a strong and persistent meridional gradient in mean atmospheric $\delta^{18}\text{O}$, with higher values towards the pole, and this is a large driver of isotopic variability in idealized simulations (Dütsch et al., 2016).

The so-called continental effect (Winnick et al., 2014), often appears as an important term driving $\delta^{18}\text{O}$ (Good et al., 2014, e.g.). Here, the fraction of the retroplume over land, f_l (calculated after 3 h of travel), has the expected sign making our results consistent with isotopic depletion driven by rainout. But, on the whole, f_l is of only minor importance because the vast majority of trajectories do not pass over land before arriving at the rainfall site. Because of the lack of overland trajectories in the data, it is unlikely that the GAM has been able to learn an accurate relationship.

Also present in the GAM is the evaporation-weighted sea surface temperature, T_s . As indicated by the dashed line in Fig. 6G, this term is consistent with the temperature dependence of equilibrium fractionation of water vapor from the ocean surface (Majoube, 1971; Horita & Wesolowski, 1994), though the presence of latitude in the model (strongly correlated with T_s) means that this relationship may be distorted.

Notably absent from the GAM is the planetary boundary layer (PBL) humidity on the day of rainfall collection (Fig. 6H). This parameter has the potential to affect the degree of rain droplet re-evaporation, and therefore rainfall isotopes, and was the leading parameter affecting $\delta^{18}\text{O}$ at an arid inland site in Eastern Australia (Crawford et al., 2017). Both sites are at a similar latitude, so Calgardup Cave’s location on the coast is likely to be the reason for the absence of a link between PBL humidity and $\delta^{18}\text{O}$.

5.2 Physical processes driving deuterium excess

The strongest predictor of daily d is the source humidity, h_s , although the relationship between d and h_s shows a lower slope (-30%) than seen in studies of water vapor; the dashed line in Fig. 9b shows a typical slope of -54% (Pfahl & Sodemann, 2014). There are three potential explanations for this. First, this difference may be due to uncertainty in the h_s estimate. The standard deviation of the difference between FLEXPART and FLEXPART-WRF derived values, accounting for part of the uncertainty, is 0.04 which is large enough, based on tests with synthetic data, to reduce the slope of the line of best fit. Second, low humidity air during rainfall (small h) causes strong re-evaporation of rainfall (Risi et al., 2008). At this coastal site, h is correlated with h_s ($R = 0.33$), so the two effects together act to reduce the observed slope between h_s and d . Third, the slope between d and h_s may be a genuine trait of the source region. Steen-Larsen et al. (2014) report a flatter slope for the $d \sim h_s$ relationship, with a slope of -42.6% , and Aemisegger and Sjolte (2018) demonstrate the $d \sim h_s$ slope varies by region. Even accounting for regional variation however, -30% is sufficiently outside the range of other observations that a combination of the other factors too, h_s uncertainty or $h \sim h_s$ correlation, is likely to be important.

The effect of sea surface temperature, T_s , and wind speed, u_{10} , have been investigated in the past and their importance is still debated. Uemura et al. (2008) reported a positive correlation between d and T_s in field measurements, in agreement with Bonne et al. (2019), whereas Pfahl and Sodemann (2014) argue that the T_s is of minor importance compared with h_s . Figure 9d shows that our data do indicate a positive correlation between d and T_s for $T_s < 20^\circ\text{C}$. The reversal at higher temperatures is physically implausible and likely to be an artifact caused by the sparse data at higher temperatures and correlation between T_s and latitude.

The relationship between u_{10} and d is weak in the GAM, and arguably inconsistent with the widely-applied results of Merlivat (1978a), in which kinetic fractionation, and hence d in evaporation, is lower at high wind speeds. In their parametrization, low

594 wind speeds below about 7 ms^{-1} correspond to a smooth regime (and higher d) whereas
 595 high wind speeds are modelled by a rough regime (with lower d) (Merlivat & Jouzel, 1979).
 596 The u_{10} relationship here is too weak to match the parametrization, it disappears from
 597 the model when synoptic types are included, and there is little evidence from other stud-
 598 ies of the Merlivat (1978a) parametrization being directly applicable in the field. Benetti
 599 et al. (2014) present data which lies between the rough and smooth, Steen-Larsen et al.
 600 (2014) find no statistical difference in d in low versus high winds, and Bonne et al. (2019)
 601 also find there to be no effect on d from wind speed, with their data being best explained
 602 by the rough regime of the Merlivat and Jouzel (1979) model. Considered in the con-
 603 text of these other studies, then, the existence of a strong relationship between d and
 604 u_{10} seems unlikely.

605 5.3 Generalizability of the model

606 As a test of the model’s performance away from the observation site, predictions
 607 of $\delta^{18}\text{O}$ for Perth Airport were computed based on observed daily rainfall and FLEX-
 608 PART backwards plumes terminating at Perth Airport on each rain day. GAM predic-
 609 tions were clipped to the range of observations to prevent extrapolation errors. In par-
 610 ticular, on days with less than 2 mm of rainfall $\delta^{18}\text{O}$ was set to the same value as if 2 mm
 611 of rainfall was observed. This was necessary because many of the monthly accumulations
 612 included a nontrivial contribution from days with light rainfall.

613 When compared with monthly $\delta^{18}\text{O}$ observations, the GAM performed well dur-
 614 ing the wet months but had large errors during the dry months (Fig. S5). On some oc-
 615 casions, this was because of highly depleted rainfall sourced from the ocean off the north-
 616 west coast of Western Australia which had made a long transit over land. In general, the
 617 failure of the model to perform well during the summer months can be attributed to lack
 618 of summer rainfall in the training data. The stronger influence of tropical processes in
 619 summer, on Perth rainfall, may also play a role.

620 When aggregated to annual data, the poor performance during the dry months be-
 621 comes inconsequential and the model generalizes well; performance in Perth shows a sim-
 622 ilar predictive skill to Calgardup Cave (Fig. S6). Furthermore, the GAM is able to re-
 623 produce the offset in mean $\delta^{18}\text{O}$ observed between Perth and Calgardup Cave. To re-
 624 produce the offset, the model needs to include rainfall intensity, rainfall along the retro-
 625 plume, source humidity, and source latitude. This suggests that a combination of these
 626 variables is responsible for the observed offset, but it also turned out that rainfall inten-
 627 sity, being responsible for about 10% of the offset, is not the main driver of the offset.
 628 The good performance of the model for the Perth observations makes it more promis-
 629 ing for the interpretation of longer-term data from the coastal zone between Calgardup
 630 and Perth.

631 For deuterium excess, GAM predictions at Perth Airport show a similar error to
 632 the Calgardup Cave timeseries tending to have a low bias at the start of the observation
 633 period and a high bias towards the end.

634 5.4 Interpretation of water isotopes in paleoclimate studies

635 Based on data from the 13 year observing period, this study confirms that rain-
 636 fall intensity is a primary driver of $\delta^{18}\text{O}$ in precipitation. The nonlinear relationship can
 637 be approximated as

$$638 \delta^{18}\text{O} = \begin{cases} \alpha \log(P/P_0) + \beta, & P \geq 2 \text{ mm day}^{-1} \\ -2.05\text{‰}, & P < 2 \text{ mm day}^{-1}, \end{cases} \quad (3)$$

639 where $P_0 = 1 \text{ mm day}^{-1}$, $\alpha = -2.85\text{‰}$, and $\beta = -1.19\text{‰}$. Importantly, years with
 640 more intense rainfall are not necessarily wetter overall. In our data, rainfall intensity (pre-
 cipitation weighted) has a weak correlation with annual rainfall ($R = 0.23$).

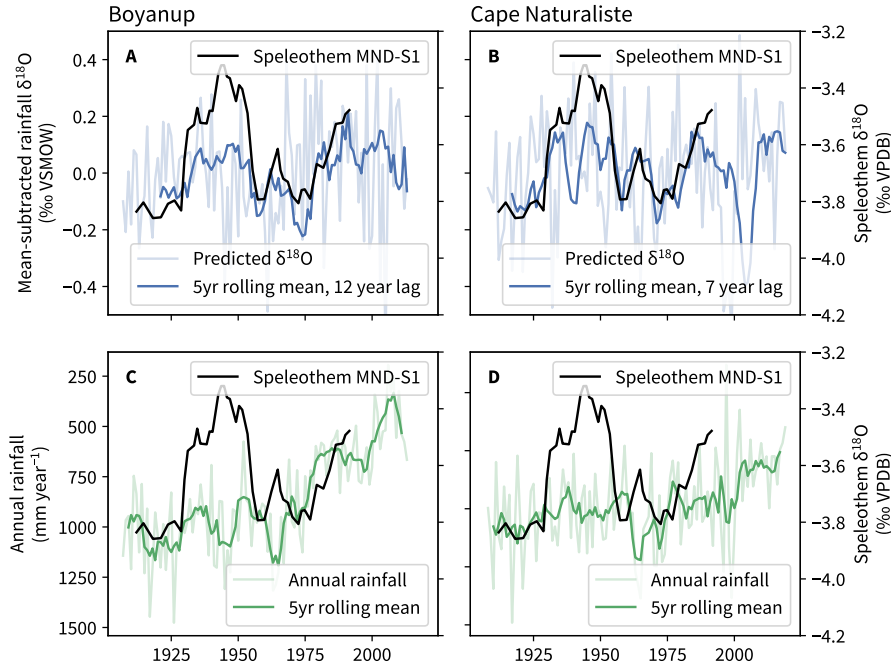


Figure 10. Speleothem MND-S1 from Moondyne Cave $\delta^{18}\text{O}$ (Treble, Chappell, et al., 2005) compared with **A** rainfall $\delta^{18}\text{O}$ inferred from Boyanup rainfall intensity, **B** Boyanup annual rainfall, **C** rainfall $\delta^{18}\text{O}$ inferred from Cape Naturaliste rainfall intensity, **D** Cape Naturaliste annual rainfall. A lag of 12 yr and smoothing with a 5 yr rolling mean has been applied to the inferred $\delta^{18}\text{O}$ timeseries for comparison with the lower resolution speleothem record which contains both analytical smoothing and attenuation due to karst flow paths. The y -axis for annual total rainfall is inverted to facilitate comparison with the speleothem $\delta^{18}\text{O}$ values.

641 In Fig. 10 we use 100 yr records of daily rainfall, along with Eq. 3, to hindcast the
 642 $\delta^{18}\text{O}$ timeseries at Boyanup and Cape Naturaliste and compare the $\delta^{18}\text{O}$ hindcast to a
 643 speleothem record from Moondyne Cave to the south (Treble, Chappell, et al., 2005).
 644 Although not the closest observations stations to the cave where the speleothem was col-
 645 lected, these are high quality stations (Lavery et al., 1997) in the Australian network (lo-
 646 cations shown in Fig. 1) meaning they are sites with long observation records and have
 647 been screened for spurious trends. To generate the hindcast, we used only days marked
 648 in the record as single-day accumulations, and checked for a weekday dependence to avoid
 649 some known quality problems in the Australian record (Viney & Bates, 2004).

650 Although taking only the leading predictor into account, rainfall $\delta^{18}\text{O}$ inferred from
 651 the Boyanup record displays an intriguing similarity to the Moondyne Cave record, par-
 652 ticularly the period of relatively higher speleothem $\delta^{18}\text{O}$ from 1930–55 and the upwards
 653 shift from the mid 1970s. There is also a marked similarity when rainfall intensity is taken
 654 from the Cape Naturaliste record, although with a divergence during the 1930–55 pe-
 655 riod. The disagreement which remains may be the result of nonlinear filtering caused by
 656 karst hydrological processes, which has only been accounted for crudely here by a com-
 657 bination of temporal averaging and introducing a time lag. Indeed the time lag, of 12
 658 or 7 years, is longer than suggested by the field evidence which perhaps indicates that
 659 uncertainties in the chronology play a role (Nagra et al., 2016, report a 5 year mismatch
 660 between the counting method and the documented history of the speleothem). Another
 661 complication is that changes in rainfall intensity, inferred from the instrumental record

(Philip & Yu, 2020), are not spatially smooth and, as demonstrated in Fig. 3, even at the annual scale the $\delta^{18}\text{O}$ timeseries is sensitive to the heaviest events which would impact sites differently, even over short spatial scales.

Supporting the interpretation that rainfall intensity is key to determining $\delta^{18}\text{O}$, on daily through to decadal timescales, the trends in annual rainfall accumulations show a weaker relationship with $\delta^{18}\text{O}$ (Fig. 10c and 10d). Post 1970, for the Boyanup hind-cast, a drying trend coincides with a upwards shift in speleothem $\delta^{18}\text{O}$. This may be a sign that the interaction between karst hydrology and $\delta^{18}\text{O}$ changes as the system dries out, but needs detailed investigation before making firm conclusions.

The link between $\delta^{18}\text{O}$ and rainfall intensity makes $\delta^{18}\text{O}$ more sensitive to extreme events than would otherwise be the case. In particular, $\delta^{18}\text{O}$ is more sensitive to extreme events than rainfall accumulations, and therefore is not as smooth spatially. This has implications for the degree of agreement that can be expected between nearby sites, especially over periods of a few decades, because the heaviest few events each year will be sampled differently at different sites. A sustained change in intense rainfall events could be further amplified by karst flowpaths as intense rainfall events are likely to be more effective at initiating recharge of karst stores (Treble et al., 2013).

In the case of deuterium excess, the interpretation of multidecadal records in this region continues to be hampered by an incomplete understanding of governing processes. The strongest predictor on a daily scale, source humidity, makes model predictions worse on an interannual scale. Out of the predictors that we considered, rainfall intensity, measured at the collection site but not along the retroplume, has the strongest effect on d . If this relationship holds over longer timeseries, it would drive an anticorrelation between d and $\delta^{18}\text{O}$. Such an anticorrelation was indeed reported by Priestley et al. (2020), in a 35 ka groundwater record, and supports the interpretation by Priestley et al that variations in groundwater isotopes through time, for the Perth Basin, are driven by precipitation intensity.

6 Conclusions

Water isotopes in precipitation were measured daily over thirteen years (2006–18). Daily variability was found to be superimposed on weaker low-frequency trends driven by anomalous conditions in the first three years of monitoring: $\delta^{18}\text{O}$ decreases by $0.06 \pm 0.03 \text{‰yr}^{-1}$ and d increases by $0.24 \pm 0.07 \text{‰yr}^{-1}$, and trends tend to weaken or reverse in the second half of the monitoring period. The factors which drive $\delta^{18}\text{O}$ and d variability, on a range of timescales, were investigated using generalized additive models (GAMs), with upstream conditions diagnosed with backwards dispersion modelling and synoptic types determined using a statistical method. Although water isotopes demonstrated an association with synoptic types, these were ultimately not a strong driver of variability because, we infer, the synoptic types contained redundant information which was better expressed by continuous values derived from retroplume diagnostics.

Daily variability in $\delta^{18}\text{O}$ was driven primarily by rainfall intensity, both at the measurement site and upstream, in agreement with the main finding of Fischer and Treble (2008), which was based on a smaller data set. The $\delta^{18}\text{O}$ seasonal cycle was driven by seasonal changes in both rainfall intensity and source humidity. The relationship between rainfall intensity, at a daily scale, and $\delta^{18}\text{O}$ was robust. It applied at both the primary measurement station, Calgardup Cave, and to monthly accumulations from Perth Airport. The relationship also appears to be robust over longer time periods, as shown by projecting the $\delta^{18}\text{O} \propto \log(P/P_0)$ relationship back through the ~ 100 yr period with rainfall observations and comparing to a speleothem record. Because of the relationship between rainfall intensity and $\delta^{18}\text{O}$, annual accumulations of $\delta^{18}\text{O}$ are more sensitive to the heaviest rainfall events each year than annual accumulated rainfall is, which has im-

712 plications both for the interpretation of $\delta^{18}\text{O}$ records and for how much nearby sites can
713 be expected to agree with each other.

714 Deuterium excess, d , differed from $\delta^{18}\text{O}$ in several respects. On a daily scale, vari-
715 ability was driven primarily by h_s , although with a flatter slope than reported in stud-
716 ies of water vapor. The d seasonal cycle was also well explained mainly by h_s , with a weaker
717 contribution from rainfall intensity. In contrast, year-to-year changes in h_s failed to ex-
718 plain the interannual signal in annual mean d , with the implication that multi-decadal,
719 or longer, records of d should not be interpreted as a proxy record of h_s in this region.
720 Furthermore, the link between rainfall intensity and d was too weak to drive the observed
721 changes in d , meaning that the driver for low-frequency changes in d was not fully ex-
722 plained. Further investigation of d is warranted; d is not as sensitive as $\delta^{18}\text{O}$ to extreme
723 events, there is a low-frequency signal in the observations at both Calgardup Caves and
724 Perth which may be climate-related; meaning that the d signal carries information which
725 supplements $\delta^{18}\text{O}$.

726 7 Acknowledgements

727 The outcomes of this study contribute to ARC DP200100203 awarded to PCT. Wa-
728 ter isotope measurements were undertaken at ANSTO and simulations were carried out
729 at ANSTO's High Performance Computing facility. We gratefully acknowledge the as-
730 sistance from the staff at Calgardup Caves (Department of Biodiversity, Conservations
731 and Attractions) to conduct the cave monitoring. IsoGSM data which appears in this
732 article was provided thanks to Kei Yoshimura. We also acknowledge the contributors to
733 open-source software used in this project, especially: R; mgcv; Python; Pandas; SOM-
734 PAK; and QGIS.

735 8 Data availability

736 The water isotope measurements from Calgardup Cave will be archived with the
737 Global Network for Isotopes in Precipitation (GNIP) should this manuscript be accepted
738 for publication (<https://www.iaea.org/services/networks/gnip>). Water isotopes measured
739 at Perth Airport are available through GNIP, <https://openscience.ansto.gov.au/collection/881>.
740 The models used in this study are available for download from <http://www.flexpart.eu/>
741 (FLEXPART and FLEXPART-WRF) and <http://www.mmm.ucar.edu/wrf/users/> (WRF).
742 Reanalysis data are archived by the European Centre for Medium Range Weather Fore-
743 casting (ERA-Interim, [https://www.ecmwf.int/en/forecasts/datasets/reanalysis-datasets/era-](https://www.ecmwf.int/en/forecasts/datasets/reanalysis-datasets/era-interim)
744 [interim](https://www.ecmwf.int/en/forecasts/datasets/reanalysis-datasets/era-interim)) and the National Oceanic and Atmospheric Administration (CFSR, [https://www.ncdc.noaa.gov/data-](https://www.ncdc.noaa.gov/data-access/model-data/model-datasets/climate-forecast-system-version2-cfsv2)
745 [access/model-data/model-datasets/climate-forecast-system-version2-cfsv2](https://www.ncdc.noaa.gov/data-access/model-data/model-datasets/climate-forecast-system-version2-cfsv2)).

746 References

- 747 Aemisegger, F., & Sjolte, J. (2018). A Climatology of Strong Large-Scale
748 Ocean Evaporation Events. Part II: Relevance for the Deuterium Excess
749 Signature of the Evaporation Flux. *J. Climate*, *31*(18), 7313–7336. doi:
750 10.1175/JCLI-D-17-0592.1
- 751 Aemisegger, F., Spiegel, J. K., Pfahl, S., Sodemann, H., Eugster, W., & Wernli, H.
752 (2015). Isotope meteorology of cold front passages: A case study combining
753 observations and modeling. *Geophys. Res. Lett.*, *42*(13), 5652–5660. doi:
754 10.1002/2015GL063988
- 755 Aggarwal, P. K., Alduchov, O. A., Froehlich, K. O., Araguas-Araguas, L. J., Stur-
756 chio, N. C., & Kurita, N. (2012). Stable isotopes in global precipitation: A
757 unified interpretation based on atmospheric moisture residence time. *Geophys.*
758 *Res. Lett.*, *39*(11). doi: 10.1029/2012GL051937
- 759 Aggarwal, P. K., Romatschke, U., Araguas-Araguas, L., Belachew, D., Longstaffe,

- 760 F. J., Berg, P., . . . Funk, A. (2016). Proportions of convective and stratiform
761 precipitation revealed in water isotope ratios. *Nature Geosci*, *9*(8), 624–629.
762 doi: 10.1038/ngeo2739
- 763 Baldini, L. M., McDermott, F., Baldini, J. U. L., Fischer, M. J., & Möllhoff, M.
764 (2010). An investigation of the controls on Irish precipitation $\delta^{18}\text{O}$ val-
765 ues on monthly and event timescales. *Clim Dyn*, *35*(6), 977–993. doi:
766 10.1007/s00382-010-0774-6
- 767 Barras, V., & Simmonds, I. (2008). Synoptic controls upon $\delta^{18}\text{O}$ in southern Tasma-
768 nian precipitation. *Geophys. Res. Lett.*, *35*(2). doi: 10.1029/2007GL031835
- 769 Barras, V., & Simmonds, I. (2009). Observation and modeling of stable water iso-
770 topes as diagnostics of rainfall dynamics over southeastern Australia. *J. Geo-*
771 *phys. Res. Atmospheres*, *114*(D23), D23308. doi: 10.1029/2009JD012132
- 772 Bates, B. C., Hope, P., Ryan, B., Smith, I., & Charles, S. (2008). Key findings from
773 the Indian Ocean Climate Initiative and their impact on policy development in
774 Australia. *Clim. Change*, *89*(3), 339–354.
- 775 Benetti, M., Reverdin, G., Pierre, C., Merlivat, L., Risi, C., Steen-Larsen, H. C., &
776 Vimeux, F. (2014). Deuterium excess in marine water vapor: Dependency on
777 relative humidity and surface wind speed during evaporation. *J. Geophys. Res.*
778 *Atmos.*, *119*(2), 584–593. doi: 10.1002/2013JD020535
- 779 Bonne, J.-L., Behrens, M., Meyer, H., Kipfstuhl, S., Rabe, B., Schöncke, L., . . .
780 Werner, M. (2019). Resolving the controls of water vapour isotopes in the
781 Atlantic sector. *Nat Commun*, *10*(1), 1–10. doi: 10.1038/s41467-019-09242-6
- 782 Brioude, J., Arnold, D., Stohl, A., Cassiani, M., Morton, D., Seibert, P., . . .
783 Wotawa, G. (2013). The Lagrangian particle dispersion model FLEXPART-
784 WRF version 3.1. *Geosci. Model Dev.*, *6*(6), 1889–1904. doi: 10.5194/
785 gmd-6-1889-2013
- 786 Brook, E. J., & Buizert, C. (2018). Antarctic and global climate history viewed from
787 ice cores. *Nature*, *558*(7709), 200. doi: 10.1038/s41586-018-0172-5
- 788 Cai, W., Shi, G., & Li, Y. (2005). Multidecadal fluctuations of winter rainfall over
789 southwest Western Australia simulated in the CSIRO Mark 3 coupled model.
790 *Geophys. Res. Lett.*, *32*(12). doi: 10.1029/2005GL022712
- 791 Chen, Z., Auler, A. S., Bakalowicz, M., Drew, D., Griger, F., Hartmann, J., . . .
792 Goldscheider, N. (2017). The World Karst Aquifer Mapping project: Concept,
793 mapping procedure and map of Europe. *Hydrogeol J*, *25*(3), 771–785. doi:
794 10.1007/s10040-016-1519-3
- 795 Comas-Bru, L., Rehfeld, K., Roesch, C., Amirnezhad-Mozhdehi, S., Harrison, S. P.,
796 Atsawawaranunt, K., . . . SISAL Working Group members (2020). SISALv2: A
797 comprehensive speleothem isotope database with multiple age–depth models.
798 *Earth Syst. Sci. Data*, *12*(4), 2579–2606. doi: 10.5194/essd-12-2579-2020
- 799 Craig, H. (1961). Isotopic Variations in Meteoric Waters. *Science*, *133*(3465), 1702–
800 1703. doi: 10.1126/science.133.3465.1702
- 801 Crawford, J., Hollins, S. E., Meredith, K. T., & Hughes, C. E. (2017). Precipitation
802 stable isotope variability and subcloud evaporation processes in a semi-arid
803 region. *Hydrol. Process.*, *31*(1), 20–34. doi: 10.1002/hyp.10885
- 804 Dansgaard, W. (1964). Stable isotopes in precipitation. *Tellus*, *16*(4), 436–468. doi:
805 10.3402/tellusa.v16i4.8993
- 806 Dee, D. P., Uppala, S. M., Simmons, A. J., Berrisford, P., Poli, P., Kobayashi, S., . . .
807 Vitart, F. (2011). The ERA-Interim reanalysis: Configuration and performance
808 of the data assimilation system. *Q.J.R. Meteorol. Soc.*, *137*(656), 553–597. doi:
809 10.1002/qj.828
- 810 Deininger, M., Werner, M., & McDermott, F. (2016). North Atlantic Oscillation
811 controls on oxygen and hydrogen isotope gradients in winter precipitation
812 across Europe; implications for palaeoclimate studies. *Clim. Past*, *12*(11),
813 2127–2143. doi: 10.5194/cp-12-2127-2016
- 814 Dey, R., Lewis, S. C., Arblaster, J. M., & Abram, N. J. (2019). A review of past and

- 815 projected changes in Australia’s rainfall. *Wiley Interdiscip. Rev. Clim. Change*,
816 *10*(3), e577. doi: 10.1002/wcc.577
- 817 Dütsch, M., Pfahl, S., & Sodemann, H. (2017). The impact of nonequilibrium and
818 equilibrium fractionation on two different deuterium excess definitions. *J. Geo-*
819 *phys. Res. Atmospheres*, *122*(23), 12,732–12,746. doi: 10.1002/2017JD027085
- 820 Dütsch, M., Pfahl, S., & Wernli, H. (2016). Drivers of $\delta^2\text{H}$ variations in an idealized
821 extratropical cyclone. *Geophys. Res. Lett.*, *43*(10), 5401–5408. doi: 10.1002/
822 2016GL068600
- 823 England, M. H., Ummenhofer, C. C., & Santoso, A. (2006). Interannual rainfall
824 extremes over southwest Western Australia linked to Indian Ocean climate
825 variability. *J. Climate*, *19*(10), 1948–1969. doi: 10.1175/JCLI3700.1
- 826 Eriksson, E. (1965). Deuterium and oxygen-18 in precipitation and other natural
827 waters Some theoretical considerations1. *Tellus*, *17*(4), 498–512. doi: 10.1111/
828 j.2153-3490.1965.tb00212.x
- 829 Farlin, J., Lai, C.-T., & Yoshimura, K. (2013). Influence of synoptic weather
830 events on the isotopic composition of atmospheric moisture in a coastal city
831 of the western United States. *Water Resour. Res.*, *49*(6), 3685–3696. doi:
832 10.1002/wrcr.20305
- 833 Fischer, M. J., & Treble, P. C. (2008). Calibrating climate- $\delta^{18}\text{O}$ regression models
834 for the interpretation of high-resolution speleothem $\delta^{18}\text{O}$ time series. *J. Geo-*
835 *phys. Res.-Atmospheres*, *113*(D17). doi: 10.1029/2007JD009694
- 836 Fohlmeister, J., Schröder-Ritzrau, A., Scholz, D., Spötl, C., Riechelmann, D. F. C.,
837 Mudelsee, M., . . . Mangini, A. (2012). Bunker Cave stalagmites: An archive
838 for central European Holocene climate variability. *Clim. Past*, *8*(5), 1751–
839 1764. doi: 10.5194/cp-8-1751-2012
- 840 Foley, G. R., & Hanstrum, B. N. (1994). The capture of tropical cyclones by cold
841 fronts off the west coast of Australia. *Wea. Forecasting*, *9*(4), 577–592. doi: 10
842 .1175/1520-0434(1994)009(0577:TCOTCB)2.0.CO;2
- 843 Forster, C., Stohl, A., & Seibert, P. (2007). Parameterization of convective trans-
844 port in a Lagrangian particle dispersion model and its evaluation. *J. Appl. Me-*
845 *teorol. Climatol.*, *46*(4), 403–422. doi: 10.1175/JAM2470.1
- 846 Frederiksen, J. S., & Frederiksen, C. S. (2007). Interdecadal changes in southern
847 hemisphere winter storm track modes. *Tellus Dyn. Meteorol. Oceanogr.*, *59*(5),
848 599–617. doi: 10.1111/j.1600-0870.2007.00264.x
- 849 Geoscience Australia. (2012). *Surface Geology of Australia, 1:1 000 000 scale, 2012*
850 *edition*. <http://data.bioregionalassessments.gov.au/dataset/8284767e-b5b1-4d8b-b8e6-b334fa972611>.
851
- 852 Geoscience Australia, & Australian Stratigraphy Commission. (2017). *Australian*
853 *Stratigraphic Units Database*. [http://www.ga.gov.au/products-services/data-](http://www.ga.gov.au/products-services/data-applications/reference-databases/stratigraphic-units.html)
854 [applications/reference-databases/stratigraphic-units.html](http://www.ga.gov.au/products-services/data-applications/reference-databases/stratigraphic-units.html).
- 855 Good, S. P., Mallia, D. V., Lin, J. C., & Bowen, G. J. (2014). Stable isotope
856 analysis of precipitation samples obtained via crowdsourcing reveals the spa-
857 tiotemporal evolution of Superstorm Sandy. *PLoS ONE*, *9*(3), e91117. doi:
858 10.1371/journal.pone.0091117
- 859 Guan, H., Zhang, X., Skrzypek, G., Sun, Z., & Xu, X. (2013). Deuterium excess
860 variations of rainfall events in a coastal area of South Australia and its rela-
861 tionship with synoptic weather systems and atmospheric moisture sources. *J.*
862 *Geophys. Res. Atmospheres*, *118*(2), 1123–1138. doi: 10.1002/jgrd.50137
- 863 Haylock, M., & Nicholls, N. (2000). Trends in extreme rainfall indices for an up-
864 dated high quality data set for Australia, 1910–1998. *Int. J. Climatol.*, *20*(13),
865 1533–1541. doi: 10.1002/1097-0088(20001115)20:13<1533::AID-JOC586>3.0.CO;
866 2-J
- 867 Hollins, S. E., Hughes, C. E., Crawford, J., Cendón, D. I., & Meredith, K. T. (2018).
868 Rainfall isotope variations over the Australian continent – Implications for
869 hydrology and isoscape applications. *Science of The Total Environment*, *645*,

- 870 630–645. doi: 10.1016/j.scitotenv.2018.07.082
- 871 Hope, P., Drosowsky, W., & Nicholls, N. (2006). Shifts in the synoptic systems in-
872 fluencing southwest Western Australia. *Clim. Dyn.*, *26*(7-8), 751–764. doi: 10
873 .1007/s00382-006-0115-y
- 874 Hope, P., Keay, K., Pook, M., Catto, J., Simmonds, I., Mills, G., . . . Berry, G.
875 (2014). A comparison of automated methods of front recognition for climate
876 studies: A case study in southwest Western Australia. *Mon. Wea. Rev.*,
877 *142*(1), 343–363. doi: 10.1175/MWR-D-12-00252.1
- 878 Horita, J., & Wesolowski, D. J. (1994). Liquid-vapor fractionation of oxygen
879 and hydrogen isotopes of water from the freezing to the critical temperature.
880 *Geochimica et Cosmochimica Acta*, *58*(16), 3425–3437.
- 881 Hughes, C. E., & Crawford, J. (2012). A new precipitation weighted method for
882 determining the meteoric water line for hydrological applications demonstrated
883 using Australian and global GNIP data. *Journal of Hydrology*, *464-465*, 344–
884 351. doi: 10.1016/j.jhydrol.2012.07.029
- 885 IAEA. (2006). *Reference sheet for international measurement standards* (Tech.
886 Rep.). Vienna, Austria.
- 887 Kohonen, T., Hynninen, J., Kangas, J., & Laaksonen, J. (1996).
888 *SOM_PAK: The Self-Organizing Map Program Package*.
889 [https://www.semanticscholar.org/paper/SOM_PAK%3A-](https://www.semanticscholar.org/paper/SOM_PAK%3A-The-Self-Organizing-Map-Program-Package-Kohonen-Hynninen/7bd2bb8319a75d9140fd4c30431c7283a6b25710)
890 *The-Self-Organizing-Map-Program-Package-Kohonen-*
891 *Hynninen/7bd2bb8319a75d9140fd4c30431c7283a6b25710*.
- 892 Krklec, K., & Domínguez-Villar, D. (2014). Quantification of the impact of moisture
893 source regions on the oxygen isotope composition of precipitation over Eagle
894 Cave, central Spain. *Geochimica et Cosmochimica Acta*, *134*, 39–54. doi:
895 10.1016/j.gca.2014.03.011
- 896 Lachniet, M. S. (2009). Climatic and environmental controls on speleothem oxygen-
897 isotope values. *Quaternary Science Reviews*, *28*(5–6), 412–432. doi: 10.1016/j
898 .quascirev.2008.10.021
- 899 Lavery, B., Joung, G., & Nicholls, N. (1997). An extended high-quality historical
900 rainfall dataset for Australia. *Australian Meteorological Magazine*, *46*(1), 27–
901 38.
- 902 Lee, J.-E., & Fung, I. (2008). “Amount effect” of water isotopes and quantitative
903 analysis of post-condensation processes. *Hydrol. Process.*, *22*(1), 1–8. doi: 10
904 .1002/hyp.6637
- 905 Lee, J.-E., Fung, I., DePaolo, D. J., & Henning, C. C. (2007). Analysis of the global
906 distribution of water isotopes using the NCAR atmospheric general circulation
907 model. *J. Geophys. Res.*, *112*(D16), D16306. doi: 10.1029/2006JD007657
- 908 LeGrande, A. N., & Schmidt, G. A. (2006). Global gridded data set of the oxygen
909 isotopic composition in seawater. *Geophys. Res. Lett.*, *33*(12). doi: 10.1029/
910 2006GL026011
- 911 Liu, J., Fu, G., Song, X., Charles, S. P., Zhang, Y., Han, D., & Wang, S. (2010).
912 Stable isotopic compositions in Australian precipitation. *J. Geophys. Res.*
913 *Atmospheres*, *115*(D23), D23307. doi: 10.1029/2010JD014403
- 914 Lorrey, A., Williams, P., Salinger, J., Martin, T., Palmer, J., Fowler, A., . . . Neil,
915 H. (2008). Speleothem stable isotope records interpreted within a multi-proxy
916 framework and implications for New Zealand palaeoclimate reconstruction.
917 *Quaternary International*, *187*(1), 52–75. doi: 10.1016/j.quaint.2007.09.039
- 918 Lucas, C., Rudeva, I., Nguyen, H., Boschat, G., & Hope, P. (2021). *Variability*
919 *and Changes to the Mean Meridional Circulation in Isentropic Coordinates*
920 (Preprint). In Review. doi: 10.21203/rs.3.rs-453822/v1
- 921 Lykoudis, S. P., Kostopoulou, E., & Argiriou, A. A. (2010). Stable isotopic signature
922 of precipitation under various synoptic classifications. *Physics and Chemistry*
923 *of the Earth, Parts A/B/C*, *35*(9), 530–535. doi: 10.1016/j.pce.2009.09.002
- 924 Majoube, M. (1971). Fractionnement en oxygene-18 et en deuterium entre l’eau et

- sa vapeur. *J. Chim. phys.*, 68(10), 1423–1436.
- McCabe-Glynn, S., Johnson, K. R., Strong, C., Berkelhammer, M., Sinha, A., Cheng, H., & Edwards, R. L. (2013). Variable North Pacific influence on drought in southwestern North America since AD 854. *Nat. Geosci.*, 6(8), 617–621. doi: 10.1038/ngeo1862
- Merlivat, L. (1978a). The dependence of bulk evaporation coefficients on air-water interfacial conditions as determined by the isotopic method. *J. Geophys. Res.*, 83(C6), 2977–2980. doi: 10.1029/JC083iC06p02977
- Merlivat, L. (1978b). Molecular diffusivities of H₂¹⁶O, HD¹⁶O, and H₂¹⁸O in gases. *The Journal of Chemical Physics*, 69(6), 2864–2871. doi: 10.1063/1.436884
- Merlivat, L., & Jouzel, J. (1979). Global climatic interpretation of the deuterium-oxygen 18 relationship for precipitation. *J. Geophys. Res.*, 84(C8), 5029–5033. doi: 10.1029/JC084iC08p05029
- Moerman, J. W., Cobb, K. M., Adkins, J. F., Sodemann, H., Clark, B., & Tuen, A. A. (2013). Diurnal to interannual rainfall $\delta^{18}\text{O}$ variations in northern Borneo driven by regional hydrology. *Earth and Planetary Science Letters*, 369–370, 108–119. doi: 10.1016/j.epsl.2013.03.014
- Moore, M., Kuang, Z., & Blossey, P. N. (2014). A moisture budget perspective of the amount effect. *Geophys. Res. Lett.*, 41(4), 1329–1335. doi: 10.1002/2013GL058302
- Nagra, G., Treble, P. C., Andersen, M. S., Fairchild, I. J., Coleborn, K., & Baker, A. (2016). A post-wildfire response in cave dripwater chemistry. *Hydrol. Earth Syst. Sci.*, 20(7), 2745–2758. doi: 10.5194/hess-20-2745-2016
- Noone, D., & Simmonds, I. (2002). Associations between $\delta^{18}\text{O}$ of Water and Climate Parameters in a Simulation of Atmospheric Circulation for 1979–95. *J. Climate*, 15(22), 3150–3169. doi: 10.1175/1520-0442(2002)015<3150:ABOOWA>2.0.CO;2
- Okazaki, A., Satoh, Y., Tremoy, G., Vimeux, F., Scheepmaker, R., & Yoshimura, K. (2015). Interannual variability of isotopic composition in water vapor over western Africa and its relationship to ENSO. *Atmos. Chem. Phys.*, 15(6), 3193–3204. doi: 10.5194/acp-15-3193-2015
- Orland, I. J., Bar-Matthews, M., Kita, N. T., Ayalon, A., Matthews, A., & Valley, J. W. (2009). Climate deterioration in the Eastern Mediterranean as revealed by ion microprobe analysis of a speleothem that grew from 2.2 to 0.9 ka in Soreq Cave, Israel. *Quat. Res.*, 71(1), 27–35. doi: 10.1016/j.yqres.2008.08.005
- Paget, M. J. (2008). *MODIS Land data sets for the Australian region* (Tech. Rep.). Canberra: CSIRO Marine and Atmospheric Research.
- Pepler, A. S., Dowdy, A. J., van Rensch, P., Rudeva, I., Catto, J. L., & Hope, P. (2020). The contributions of fronts, lows and thunderstorms to southern Australian rainfall. *Clim Dyn.*, 55(5), 1489–1505. doi: 10.1007/s00382-020-05338-8
- Pfahl, S., & Sodemann, H. (2014). What controls deuterium excess in global precipitation? *Clim. Past*, 10(2), 771–781. doi: 10.5194/cp-10-771-2014
- Pfahl, S., & Wernli, H. (2008). Air parcel trajectory analysis of stable isotopes in water vapor in the eastern Mediterranean. *J. Geophys. Res. Atmospheres*, 113(D20), D20104. doi: 10.1029/2008JD009839
- Pfahl, S., & Wernli, H. (2009). Lagrangian simulations of stable isotopes in water vapor: An evaluation of nonequilibrium fractionation in the Craig-Gordon model. *J. Geophys. Res.*, 114(D20), D20108.
- Philip, P., & Yu, B. (2020). Interannual variations in rainfall of different intensities in South West of Western Australia. *Int. J. Climatol.*, 40(6), 3052–3071. doi: 10.1002/joc.6382
- Philipp, A., Beck, C., Huth, R., & Jacobeit, J. (2016). Development and comparison of circulation type classifications using the COST 733 dataset and software. *Int. J. Climatol.*, 36(7), 2673–2691. doi: 10.1002/joc.3920

- 980 Pook, M. J., Risbey, J. S., & McIntosh, P. C. (2012). The synoptic climatology of
 981 cool-season rainfall in the central wheatbelt of Western Australia. *Mon. Wea.*
 982 *Rev.*, *140*(1), 28–43. doi: 10.1175/MWR-D-11-00048.1
- 983 Power, S., Sadler, B., & Nicholls, N. (2005). The influence of climate science on
 984 water management in Western Australia: Lessons for climate scientists. *Bull.*
 985 *Amer. Meteor. Soc.*, *86*(6), 839–844. doi: 10.1175/BAMS-86-6-839
- 986 Priestley, S. C., Meredith, K. T., Treble, P. C., Cendón, D. I., Griffiths, A. D.,
 987 Hollins, S. E., . . . Pigois, J.-P. (2020). A 35 ka record of groundwater recharge
 988 in south-west Australia using stable water isotopes. *Sci. Total Environ.*, *717*,
 989 135105. doi: 10.1016/j.scitotenv.2019.135105
- 990 R Core Team. (2014). *R: A language and environment for statistical computing*
 991 (Tech. Rep.). Vienna, Austria.
- 992 Raut, B. A., Jakob, C., & Reeder, M. J. (2014). Rainfall changes over southwestern
 993 Australia and their relationship to the Southern Annular Mode and ENSO. *J.*
 994 *Climate*, *27*(15), 5801–5814. doi: 10.1175/JCLI-D-13-00773.1
- 995 Raut, B. A., Reeder, M. J., & Jakob, C. (2016). Trends in CMIP5 Rainfall Patterns
 996 over Southwestern Australia. *J. Climate*, *30*(5), 1779–1788. doi: 10.1175/JCLI
 997 -D-16-0584.1
- 998 Risi, C., Bony, S., & Vimeux, F. (2008). Influence of convective processes on the
 999 isotopic composition ($\delta^{18}\text{O}$ and δD) of precipitation and water vapor in the
 1000 tropics: 2. Physical interpretation of the amount effect. *J. Geophys. Res.*,
 1001 *113*(D19), D19306. doi: 10.1029/2008JD009943
- 1002 Risi, C., Bony, S., Vimeux, F., & Jouzel, J. (2010). Water-stable isotopes in
 1003 the LMDZ4 general circulation model: Model evaluation for present-day
 1004 and past climates and applications to climatic interpretations of tropical
 1005 isotopic records. *J. Geophys. Res. Atmospheres*, *115*(D12), D12118. doi:
 1006 10.1029/2009JD013255
- 1007 Risi, C., Noone, D., Worden, J., Frankenberg, C., Stiller, G., Kiefer, M., . . . Sturm,
 1008 C. (2012). Process-evaluation of tropospheric humidity simulated by general
 1009 circulation models using water vapor isotopologues: 1. Comparison between
 1010 models and observations. *J. Geophys. Res. Atmospheres*, *117*(D5). doi:
 1011 10.1029/2011JD016621
- 1012 Rudeva, I., Simmonds, I., Crock, D., & Boschat, G. (2019). Midlatitude fronts and
 1013 variability in the Southern Hemisphere tropical width. *J. Clim.*, *32*(23), 8243–
 1014 8260. doi: 10.1175/JCLI-D-18-0782.1
- 1015 Saha, S., Moorthi, S., Pan, H.-L., Wu, X., Wang, J., Nadiga, S., . . . Goldberg, M.
 1016 (2010). The NCEP Climate Forecast System Reanalysis. *Bull. Amer. Meteor.*
 1017 *Soc.*, *91*(8), 1015–1058. doi: 10.1175/2010BAMS3001.1
- 1018 Schemm, S., Rudeva, I., & Simmonds, I. (2015). Extratropical fronts in the lower
 1019 troposphere—global perspectives obtained from two automated methods. *Q. J.*
 1020 *R. Meteorol. Soc.*, *141*(690), 1686–1698. doi: 10.1002/qj.2471
- 1021 Schlosser, E., Dittmann, A., Stenni, B., Powers, J. G., Manning, K. W., Masson-
 1022 Delmotte, V., . . . Scarchilli, C. (2017). The influence of the synoptic regime
 1023 on stable water isotopes in precipitation at Dome C, East Antarctica. *The*
 1024 *Cryosphere*, *11*(5), 2345–2361. doi: 10.5194/tc-11-2345-2017
- 1025 Schmidt, G. A., LeGrande, A. N., & Hoffmann, G. (2007). Water isotope expres-
 1026 sions of intrinsic and forced variability in a coupled ocean-atmosphere model.
 1027 *J. Geophys. Res.*, *112*(D10), D10103. doi: 10.1029/2006JD007781
- 1028 Scholl, M. A., Shanley, J. B., Zegarra, J. P., & Coplen, T. B. (2009). The stable
 1029 isotope amount effect: New insights from NEXRAD echo tops, Luquillo Moun-
 1030 tains, Puerto Rico. *Water Resour. Res.*, *45*(12). doi: 10.1029/2008WR007515
- 1031 Seibert, P., & Frank, A. (2004). Source-receptor matrix calculation with a La-
 1032 grangian particle dispersion model in backward mode. *Atmos. Chem. Phys.*,
 1033 *4*(1), 51–63. doi: 10.5194/acp-4-51-2004
- 1034 Simmonds, I., Keay, K., & Tristram Bye, J. A. (2011). Identification and climatol-

- 1035 ogy of Southern Hemisphere mobile fronts in a modern reanalysis. *J. Climate*,
 1036 25(6), 1945–1962. doi: 10.1175/JCLI-D-11-00100.1
- 1037 Skamarock, W. C., & Klemp, J. B. (2008). A time-split nonhydrostatic atmospheric
 1038 model for weather research and forecasting applications. *Journal of Computa-*
 1039 *tional Physics*, 227(7), 3465–3485. doi: 10.1016/j.jcp.2007.01.037
- 1040 Smith, A., Massuel, S., Pollock, D., & Dillon, P. (2012). Geohydrology of the
 1041 Tamala Limestone Formation in the Perth Region: Origin and role of sec-
 1042 ondary porosity.
 1043 doi: 10.4225/08/599dd0fd98a44
- 1044 Sodemann, H., Schwierz, C., & Wernli, H. (2008). Interannual variability of Green-
 1045 land winter precipitation sources: Lagrangian moisture diagnostic and North
 1046 Atlantic Oscillation influence. *J. Geophys. Res. Atmospheres*, 113(D3). doi:
 1047 10.1029/2007JD008503
- 1048 Steen-Larsen, H. C., Sveinbjörnsdóttir, A. E., Peters, A. J., Masson-Delmotte, V.,
 1049 Guishard, M. P., Hsiao, G., . . . White, J. W. C. (2014). Climatic controls
 1050 on water vapor deuterium excess in the marine boundary layer of the North
 1051 Atlantic based on 500 days of in situ, continuous measurements. *Atmos. Chem.*
 1052 *Phys.*, 14(15), 7741–7756. doi: 10.5194/acp-14-7741-2014
- 1053 Stohl, A., Eckhardt, S., Forster, C., James, P., Spichtinger, N., & Seibert, P. (2002).
 1054 A replacement for simple back trajectory calculations in the interpretation
 1055 of atmospheric trace substance measurements. *Atmospheric Environment*,
 1056 36(29), 4635–4648. doi: 10.1016/S1352-2310(02)00416-8
- 1057 Sturm, K., Hoffmann, G., Langmann, B., & Stichler, W. (2005). Simulation of $\delta^{18}\text{O}$
 1058 in precipitation by the regional circulation model REMO_iso. *Hydrol. Process.*,
 1059 19(17), 3425–3444. doi: 10.1002/hyp.5979
- 1060 Treble, P. C., Bradley, C., Wood, A., Baker, A., Jex, C. N., Fairchild, I. J., . . .
 1061 Azcurra, C. (2013). An isotopic and modelling study of flow paths and stor-
 1062 age in Quaternary calcarenite, SW Australia: Implications for speleothem
 1063 paleoclimate records. *Quaternary Science Reviews*, 64, 90–103. doi:
 1064 10.1016/j.quascirev.2012.12.015
- 1065 Treble, P. C., Budd, W. F., Hope, P. K., & Rustomji, P. K. (2005). Synoptic-
 1066 scale climate patterns associated with rainfall $\delta^{18}\text{O}$ in southern Australia. *J.*
 1067 *Hydrol.*, 302(1-4), 270–282. doi: 10.1016/j.jhydrol.2004.07.003
- 1068 Treble, P. C., Chappell, J., Gagan, M. K., McKeegan, K. D., & Harrison, T. M.
 1069 (2005). In situ measurement of seasonal $\delta^{18}\text{O}$ variations and analysis of iso-
 1070 topic trends in a modern speleothem from southwest Australia. *Earth and*
 1071 *Planetary Science Letters*, 233(1–2), 17–32. doi: 10.1016/j.epsl.2005.02.013
- 1072 Tyler, J. J., Jones, M., Arrowsmith, C., Allott, T., & Leng, M. J. (2016). Spatial
 1073 patterns in the oxygen isotope composition of daily rainfall in the British Isles.
 1074 *Clim. Dyn.*, 47(5-6), 1971–1987. doi: 10.1007/s00382-015-2945-y
- 1075 Uemura, R., Matsui, Y., Yoshimura, K., Motoyama, H., & Yoshida, N. (2008).
 1076 Evidence of deuterium excess in water vapor as an indicator of ocean sur-
 1077 face conditions. *J. Geophys. Res. Atmospheres*, 113(D19), D19114. doi:
 1078 10.1029/2008JD010209
- 1079 van Breukelen, M. R., Vonhof, H. B., Hellstrom, J. C., Wester, W. C. G., & Kroon,
 1080 D. (2008). Fossil dripwater in stalagmites reveals Holocene temperature and
 1081 rainfall variation in Amazonia. *Earth and Planetary Science Letters*, 275(1),
 1082 54–60. doi: 10.1016/j.epsl.2008.07.060
- 1083 van Ommen, T. D., & Morgan, V. (2010). Snowfall increase in coastal East Antarc-
 1084 tica linked with southwest Western Australian drought. *Nat. Geosci.*, 3(4),
 1085 267–272. doi: 10.1038/ngeo761
- 1086 Viney, N. R., & Bates, B. C. (2004). It never rains on Sunday: The prevalence
 1087 and implications of untagged multi-day rainfall accumulations in the Aus-
 1088 tralian high quality data set. *Int. J. Climatol.*, 24(9), 1171–1192. doi:
 1089 10.1002/joc.1053

- 1090 Vonhof, H. B., van Breukelen, M. R., Postma, O., Rowe, P. J., Atkinson, T. C., &
 1091 Kroon, D. (2006). A continuous-flow crushing device for on-line $\delta^2\text{H}$ analysis of
 1092 fluid inclusion water in speleothems. *Rapid Commun. Mass Spectrom.*, *20*(17),
 1093 2553–2558. doi: 10.1002/rcm.2618
- 1094 Wang, S., Zhang, M., Crawford, J., Hughes, C. E., Du, M., & Liu, X. (2017).
 1095 The effect of moisture source and synoptic conditions on precipitation iso-
 1096 topes in arid central Asia. *J. Geophys. Res. Atmos.*, 2015JD024626. doi:
 1097 10.1002/2015JD024626
- 1098 Webster, C. R., & Heymsfield, A. J. (2003). Water isotope ratios D/H, $^{18}\text{O}/^{16}\text{O}$,
 1099 $^{17}\text{O}/^{16}\text{O}$ in and out of clouds map dehydration pathways. *Science*, *302*(5651),
 1100 1742–1745. doi: 10.1126/science.1089496
- 1101 Werner, M., Langebroek, P. M., Carlsen, T., Herold, M., & Lohmann, G. (2011).
 1102 Stable water isotopes in the ECHAM5 general circulation model: Toward high-
 1103 resolution isotope modeling on a global scale. *J. Geophys. Res.*, *116*(D15),
 1104 D15109. doi: 10.1029/2011JD015681
- 1105 Winnick, M. J., Chamberlain, C. P., Caves, J. K., & Welker, J. M. (2014). Quantify-
 1106 ing the isotopic ‘continental effect’. *Earth and Planetary Science Letters*, *406*,
 1107 123–133. doi: 10.1016/j.epsl.2014.09.005
- 1108 Wood, S. N. (2006). *Generalized additive models: An introduction with R*. Chapman
 1109 and Hall/CRC.
- 1110 Wood, S. N. (2011). Fast stable restricted maximum likelihood and marginal like-
 1111 lihood estimation of semiparametric generalized linear models. *J. R. Stat. Soc.*
 1112 *Ser. B Stat. Methodol.*, *73*(1), 3–36. doi: 10.1111/j.1467-9868.2010.00749.x
- 1113 Wood, S. N. (2017). *Generalized additive models: An introduction with R*. Chapman
 1114 and Hall/CRC.
- 1115 Yoshimura, K., Kanamitsu, M., Noone, D., & Oki, T. (2008). Historical isotope
 1116 simulation using Reanalysis atmospheric data. *J. Geophys. Res.*, *113*(D19),
 1117 D19108. doi: 10.1029/2008JD010074
- 1118 Zhang, H., Griffiths, M. L., Chiang, J. C. H., Kong, W., Wu, S., Atwood, A., ...
 1119 Xie, S. (2018). East Asian hydroclimate modulated by the position of
 1120 the westerlies during Termination I. *Science*, *362*(6414), 580–583. doi:
 1121 10.1126/science.aat9393
- 1122 Zhang, Z., Li, G., Yan, H., & An, Z. (2018). Microcodium in Chinese loess as a
 1123 recorder for the oxygen isotopic composition of monsoonal rainwater. *Quater-
 1124 nary International*, *464*, 364–369. doi: 10.1016/j.quaint.2017.10.050
- 1125 Zheng, Y., Jong, L. M., Phipps, S. J., Roberts, J. L., Moy, A. D., Curran, M. A. J.,
 1126 & van Ommen, T. D. (2020). Extending and understanding the South
 1127 West Western Australian rainfall record using a snowfall reconstruction
 1128 from Law Dome, East Antarctica. *Clim. Past Discuss. [preprint]*, 1–32. doi:
 1129 10.5194/cp-2020-124